

Development and application of the Ascent-Drift-Descent Radiosonde System (ADDRS)

Xiaozhong Cao¹, Qiyun Guo^{2,3,4}, Haowen Luo^{2,3,4}, Rongkang Yang^{2,3,4}, Peng Zhang^{2,3,4}, Guo Jianping⁵, Jincheng Wang⁶, Die Xiao⁷, Yinfeng Liu⁸, Zhongliang Sun⁹, Shijun Liu¹⁰, Sijie Chen¹¹, Anfan Huang^{2,3,4}

¹ China Meteorological Administration, Beijing, China;

² Meteorological Observation Centre of China Meteorological Administration, Beijing, China;

³ State Key Laboratory of Environment Characteristics and Effects for Near-space, Beijing, China;

⁴ Engineering Technology Research Center for Meteorological Observation of CMA, Beijing, China;

⁵ Chinese Academy of Meteorological Sciences, Beijing, China;

⁶ CMA Earth System Modeling and Prediction Centre (CEMC), Beijing, China;

⁷ Hunan Key Laboratory of Near-space Meteo-ballon Materials and Technology, Zhuzhou Research & Design Institute Co, Ltd, Zhuzhou, China;

⁸ Beijing Huayun Orient Detection Technology Co, Ltd., Beijing, China;

⁹ Allystar Technology (Shenzhen) Co.LTD. , Shenzhen, China;

¹⁰ Department of Advanced Technology Training of China Meteorological Administration, Beijing, China;

¹¹ National Satellite Meteorological Centre of China Meteorological Administration, Beijing, China;

Corresponding author: Xiaozhong Cao, caoxzh@cma.gov.cn

ABSTRACT. The balloon-borne radiosonde observations constitutes a crucial component of meteorological sounding, which conducts a ground to upper-air “ascent phase” sounding. This paper introduces the Ascent-Drift-Descent Radiosonde System (ADDRS), an innovative system characterized by three observation phases—'Ascent-Drift-Descent' (ADD)—in which all three phases of sounding observation are executed through single balloon launch. Several key technologies were successfully developed, including the carrier (dual-mode balloon), the payload (System-on-Chip (SoC) module for meteorological sounding), Ground to upper-air data reception and control command transmission and data processing framework based on 'Internet cloud + Instrument terminal' was established. Data quality control methods and data assimilation techniques of ADDRS were also developed. An interactive experiment encompassing observations and forecasting was conducted to evaluate the quality of experimental data at each phase of ADDRS. A numerical experiment on the impact of ADDRS data assimilation on forecasting demonstrated a 2% reduction in precipitation forecast error at 06:00 and 18:00 (UTC), along with an average 1% improvement in precipitation forecast accuracy following the assimilation of ADDRS data. Furthermore, a new trajectory prediction method for ADDRS, achieved an average simulated landing-point error of less than 40 km. Notably, the accuracy of first guess positioning and trajectory prediction for Typhoon 'Saola' in 2023 was significantly enhanced through ADDRS data assimilation, reducing the average trajectory prediction error by 40%. On January 1, 2024, operational observations using ADDRS commenced at four radiosonde observations stations in Guangdong, China. Starting in July 2024, an operational experiment at one hundred and twenty-seven stations within the China Meteorological Administration (CMA) was operation over one year, which will achieve full operational capability by 2026.

38 **1. Introduction**

39 The upper-air meteorological sounding system (hereinafter referred to as 'sounding') constitutes a key
40 element within comprehensive meteorological measurement framework (Ingleby and Coauthors., 2016). It is
41 responsible for gathering data on various meteorological elements such as temperature, humidity, pressure, wind
42 speed, and wind direction from the surface up to heights of 30 km and beyond upper atmosphere (DuBois et al.,
43 2002). This system provides vertically observed meteorological data for weather forecasting, numerical weather
44 prediction, climate projection, scientific research, and the inspection and calibration of ground-based remote
45 sensing equipment (Seidel et al., 2009; Fujiwara et al., 2025). The integration of radiosonde technology with
46 balloon-borne soundings emerged in the 1930s, with early operational systems deployed in the 1940s; this
47 technology has since served as a primary tool for direct measurements of upper-air meteorological elements
48 below 30 km and is widely utilized on a global scale (Pettifer 2009; Gallice et al., 2011).

49 For nearly a century, these radiosondes have utilized the direct measurement method of “one balloon
50 launched, one profile”. Where the radiosonde ascends at a certain speed with the balloon expanding in volume
51 due to decreasing air pressure as altitude increases. Upon reaching a specific altitude, the balloon bursts,
52 concluding the measurement process. This methodology confines effective observations to the radiosonde's
53 ascent phase (Haig et al., 1958). The disposable nature of radiosondes and balloons necessitates significant costs
54 for multiple deployments. Consequently, economic constraints have led to reductions in sounding operations,
55 such as Russia's temporary reduction of launches from twice to once daily in 2015, impacting the forecasting
56 accuracy of numerical prediction models across Northern Hemisphere countries (Ingleby et al., 2016).

57 Currently, the radiosonde observations are still very useful for validation/verification satellite observations
58 (Bauer et al.,2015; Bormann et al.,2019; WMO et al.,2024). But the temporal resolution of global radiosonde
59 observations data remains limited, posing a significant challenge to its capacity in fulfilling the requirements of
60 routine forecasting. A notable concern arises from the scarcity of direct measurement data during periods
61 characterized by frequent severe convective activity, particularly in the hours immediately following noon.
62 Numerous studies have demonstrated that the frequent acquisition of descent radiosonde data can significantly
63 enhance the accuracy of numerical weather forecasting. The ECMWF reported about successfully assimilating
64 radiosonde descent data from ships (Ingleby, 2021), And the United States and other nations have successfully
65 assimilated airborne radiosonde data into their model systems, leading to a 10–15% reduction in errors
66 associated with hurricane trajectory predictions, particularly over oceanic regions where data is sparse (Cohn et
67 al., 2013; Wang et al., 2015).

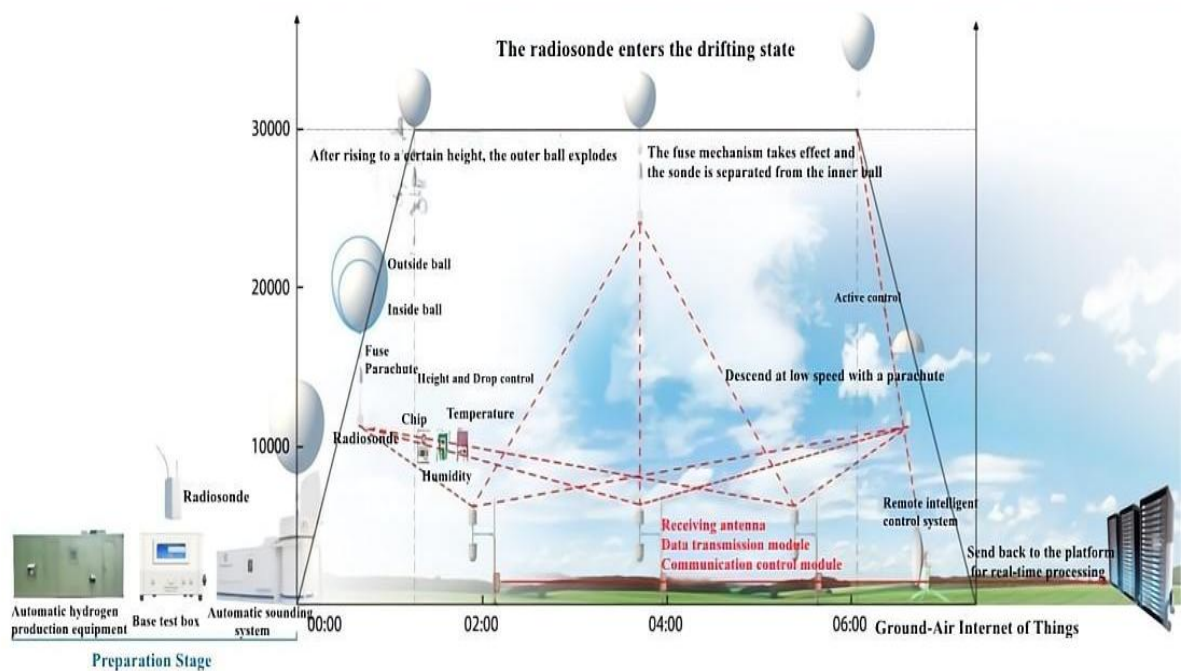
68 Additionally, numerous institutions are actively investigating techniques to obtain multiple radiosonde data
69 points from a solitary balloon launch. Illustrative projects include the multidisciplinary analysis of the African
70 monsoon and the measurement system research and forecasting experiments conducted in the Asia-Pacific
71 region, which utilize balloons to conduct drop soundings as they drift with stable upper-air winds over the
72 ocean (Raman et al., 2011). The WindBorne emerged in 2019 from the cradle of the Stanford Space Program .
73 Once launched, the WindBorne balloon regulates its altitude by jettisoning sand ballast and releasing gas,
74 enabling multiple round-trip vertical sounding flights from below 20 km down to near the surface, with an
75 average flight duration of seven days (Johnson, 2024). Similarly, the French Space Agency, CNES, has
76 developed an Super Pressure Balloon (SPB) capable of floating in the stratosphere for over three months (Roth
77 et al., 2022). Additionally, the Tata Institute of Fundamental Research Balloon Facility (TIFR-BF) in India has

78 also contributed to this field by developing comparable systems (Anand et al., 2021; Vernier et al., 2018;
 79 Vernier., 2022). The systems delineated in these studies are primarily used for scientific
 80 experiments. Nonetheless, due to high costs and limited ascent rates, they are not viable solutions for long-term
 81 operational balloon sounding data collection. Furthermore, these balloons very slow ascent rates (necessary for
 82 managing factors such as heat dissipation, ventilation, and sensor response times) do not meet WMO standards
 83 for balloon ascent speed (WMO-No. 8., 2025).

84 Another conducted an extensive analysis by compiling four years of radiosonde data collected without
 85 parachutes across various seasons and altitudes, highlighting the scientific value of descent data (Ratnam et al.,
 86 2014; Ingleby et al., 2022). On account of the sounding process of ascending and descending at the same station
 87 has restricted its potential in conducting adaptive or targeting observation on typhoon forecast (Tan et al., 2006).
 88 This paper introduce a new sounding technology—the Ascent-Drift-Descent Radiosonde System (ADDRS).
 89 This system can improve the spatial and temporal frequency of soundings and provides an additional vertical
 90 profile as well as maintaining cost-effective, which acquires radiosonde measurement data throughout three
 91 phases—'Ascent-Drift-Descent' (ADD)—all within a single balloon launch (Cao et al., 2019).

92 **2. Synopsis of the Ascent-Drift-Descent Radiosonde System (ADDRS)**

93 The ADDRS was organizational developed by the Meteorological Observation Centre of the China
 94 Meteorological Administration (MOC of CMA) with other relevant domestic units in China (hereinafter referred
 95 to as the 'ADDRS research team'). It undertakes a three-phase Round-trip upper-air measurement (Fig. 1). In
 96 addition to the ascent phase of the current sounding system, ADDRS enables sounding during both the drift and
 97 descent phases. This innovative approach completes three phases of sounding with only a single balloon launch,
 98 representing a significant advancement in comparison with the traditional upper-air sounding method that has
 99 been utilized for nearly a century (Cao et al., 2022).

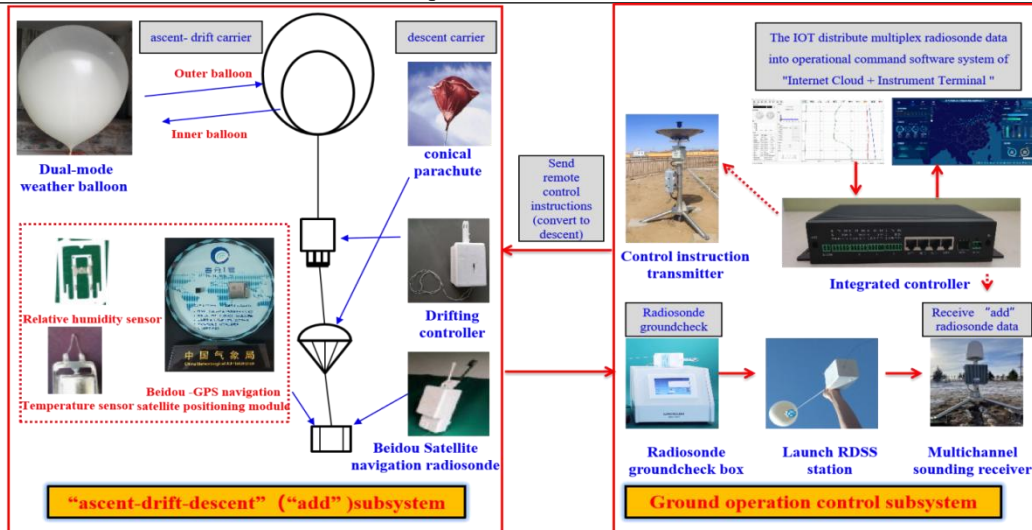


100

101 **Figure 1. Operational principle diagram of the Ascent-Drift-Descent Radiosonde System (ADDRS).**

102 **Table 1. Main instruments and key functions of ADDR5.**

No	Subsystem	Instruments	Key Function
1	“ADD” subsystem	dual-mode balloon	“outer balloon” as ascent carrier, “inner balloon” as drift carrier
2		parachute	parachute as the carrier of the descent phase
3		drifting controller	Adaptive control of drift and descent
4		radiosonde	The temperature, pressure, humidity, wind measurement meet the demand for long-term stratospheric observation
5	Ground operation control subsystem	Ground station	ground inspection ground check, balloon inflation, launch, and other tasks before the equipment is launched
6		Multichannel sounding receiver	8 channels receive radiosonde data simultaneously
7		control command transmitter	In the weather-sensitive area without a station, the active fusing drifting controller is carried out and the descent measurement is started
8		operational management system	Real-time acquisition, transmission, quality control, and timely delivery of control instructions for ADDR5 data, providing real-time high-quality data to weather analysis and numerical prediction models



103
104 **Figure 2. Schematic representation of the equipment composition for ADDR5.**

105 The ADDR5 primarily consists of the 'ADD' subsystem and the ground operational control subsystem, as
 106 shown in Table 1 and Fig. 2. The 'ADD' subsystem encompasses a dual-mode balloon with a parachute, a
 107 drifting controller, and a radiosonde. The dual-mode balloon features a design where one balloon embedded
 108 within another, both made from a latex material similar to that of operational meteorological sounding balloons
 109 and filled with hydrogen. Upon inflation and launch of the dual-mode balloon, the 'ADD' subsystem at a rate of
 110 ascent between 5 and 7 m/s (WMO-No. 8., 2025). As it rises, the external air pressure decreases, causing the
 111 balloon to expand. At the predetermined altitude (generally between 28km and 30km), the outer balloon bursts
 112 due to its expanding volume, marking the conclusion of the ascent phase measurement. Given that the outer
 113 balloon bursts within the stratosphere, where vertical air movement is minimal, horizontal movement becomes
 114 predominant. The enhanced performance and controlled aeration of the inner balloon enable it to resist bursting.
 115 At this juncture, the buoyancy of the inner balloon attains equilibrium with gravity, achieving an approximate

116 vertical stability. Subsequently, the inner balloon, primarily influenced by horizontal air currents, functions as
117 the carrier for the drift phase, which initiates thereafter.

118 After drifting for a predefined duration, which may vary from a couple of hours to over ten hours, the
119 drifting controller separates the inner balloon from the rest of the ADDRS equipment, thereby terminating the
120 drift phase. Subsequent to this separation, the inner balloon persists in ascending until it ultimately ruptures,
121 marking the conclusion of its mission segment. Meanwhile, the remaining components — comprising the
122 parachute and radiosonde—begins to descend. The parachute is promptly deployed, facilitating the radiosonde
123 in collecting data during the descent phase, while acting as its carrier. This descent persists until the equipment
124 touches down, thereby completing the final phase of the 'ADD' process. At this point, ADDRS has successfully
125 completed the three-phase 'Ascent-Drift-Descent' measurement.

126 The ground operation control subsystem of ADDRS comprises four main components: the balloon launch
127 station, ground data-receiver (downlink communication), control command transmitter (uplink communication),
128 and the operational management system. The balloon launch station is similar to existing meteorological
129 radiosonde launch stations, undertaking tasks such as ground checks, balloon inflation, and launching the
130 balloon with a radiosonde at scheduled intervals. Ground data-receiver can also be placed at the balloon launch
131 station. However, its layout and function differ from operational-sounding data-receiving equipment. Due to the
132 ADDRS drift phase, the horizontal distance between the descent point of the radiosonde and its launch point can
133 exceed 500km, while operational radiosonde data reception has a maximum linear transmission distance of
134 around 200km-300km. Therefore, the traditional single-station, point-to-point radio communication mode of
135 radiosondes is inadequate for ADDRS data reception. Thus, the ground to upper-air communication system has
136 been upgraded from point-to-point to a multiple-to-multiple model. In areas through which the radiosonde's
137 ADD phases may pass, ground data-receivers are strategically deployed. This configuration enables multiple
138 ground data-receivers to concurrently receive data from a single radiosonde or alternatively, a single receiver to
139 capture data signals from several radiosondes simultaneously. Consequently, the ground data-receiver is
140 designed as a P-band 8-channel parallel data receiver, capable of receiving data from multiple radiosondes
141 simultaneously. Additionally, control command transmitters are located at the ground station and other locations.
142 These transmitters send control instructions from the ground to the drifting controller in the air through uplink
143 communication. This system allows for the adjustment of the drift phase elevation, termination of the drift phase,
144 and switching to the descent phase measurement as needed.

145 The operational management system acts as the brain of the entire ADDRS system. Multiple ground data-
146 receivers and control command transmitters are connected to the operational management system via the
147 Internet. These ground data-receivers continuously transmit data to the operational management system in real-
148 time for processing, display, and storage. Based on the ADDRS trajectory and specific weather and climate
149 conditions, comprehensive decision-making allows the operational management system to transmit control
150 instructions to control command transmitters which then relay them to the drifting controller in the air to execute
151 the desired functions.

152 The 'Internet cloud + Instruments terminal' architecture enables real-time, efficient, and bidirectional
153 communication across the entire network during the 'ADD' phases. This configuration supports the seamless
154 real-time acquisition, transmission, and quality control of ADDRS data while ensuring rapid data delivery for

155 weather forecasting. Consequently, it enhances the timeliness and availability of radiosonde data for forecasting
 156 purposes.

157 3. Critical scientific problems

158 3.1. Carrier technology

159 Compared to using deflation in super-pressure balloons for drifting (Anand et al., 2021; Vernier et al., 2018;
 160 Vernier. et al., 2022), the dual-mode balloon structure of ADDRS is simpler, more cost-effective, and suitable
 161 for large-scale deployment in operational upper-air meteorological observations. The ideal 'ADD' process works
 162 as follows: the outer balloon provides lift and explodes after reaching a predefined altitude range. Subsequently,
 163 the inner balloon and its associated equipment achieve vertical equilibrium, enabling a stable drifting state.
 164 Therefore, while the ascent measurement of the balloon sounding is completed, achieving extended drift and
 165 controlled descent remains a technical challenge that ADDRS carriers aim to overcome.

166 3.1.1 Study on the influence of atmospheric environment on the net lift power of balloons

167 A multitude of meteorological factors, encompassing air temperature, air pressure, solar radiation, and
 168 other external environmental conditions, coupled with the gas volume of the outer balloon directly influences
 169 its net lift and burst altitude. Variations in air pressure and temperature within the outer balloon, induced by
 170 external meteorological conditions, interact with the expansion dynamics of the inner balloon. These factors, in
 171 conjunction with the aeration volume of the inner balloon, collectively influence the altitude during the drift
 172 phase and the static equilibrium of the inner balloon. Consequently, controlling the hydrogen inflation volume
 173 in the dual-mode balloon presents a significant challenge (Xu et al., 2025).

174 The ADDRS research team conducted an in-depth theoretical analysis of the ascent and drift processes of
 175 the dual-mode balloon, focusing on three areas: upper atmosphere model expansion, the balloon's dynamic
 176 equation, and a thermodynamic model. This study led to the development of a coupling model that accounts for
 177 the effects of atmospheric conditions on the balloon's net lift (from now on referred to as the "coupling model")
 178 (Liu, S. J et al., 2022). This model provides a theoretical foundation for determining the net lift force, ascent
 179 velocity, and target burst altitude of the dual-mode balloon, enabling precise control of aeration in the dual-
 180 mode balloon under varying meteorological conditions.

181 **Table 2. Aeration test results based on coupling model.**

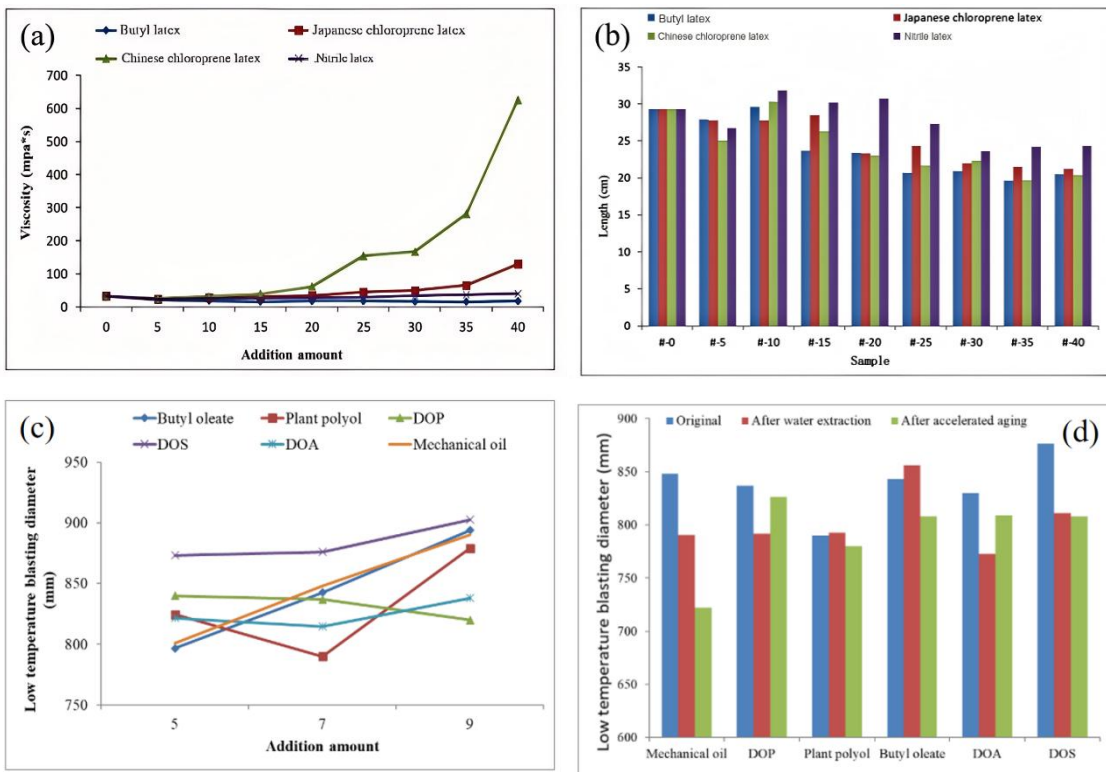
Inflatable mode	Effective launch times	Drift number of times	Drift success rate	$\geq 4h$ number of times	$\geq 4h$ success rate
Algorithm software	611	479	78.40%	436	71.36%

182 Table 2 presents data from six stations (Changsha, Wuhan, Anqing, Yichang, Nanchang, and
 183 Ganzhou) situated along the middle and lower reaches of the Yangtze River in 2021. Using the coupling model,
 184 we calculated the aeration capacities of the inner and outer balloons and determined the success rate of the dual-
 185 mode balloon launches. The results demonstrate that the coupling model effectively controls the aeration of
 186 dual-mode balloon, enabling them to achieve the intended ascent and drift measurements.

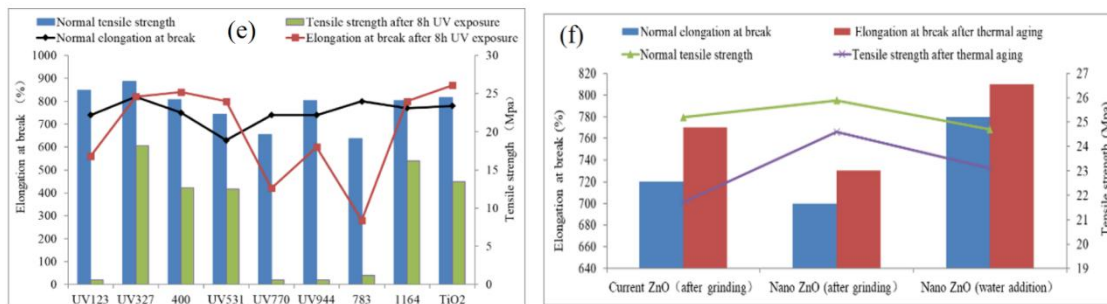
187 3.1.2 Performance improvement of the double - layer balloon

188 The ascent phase of meteorological sounding typically lasts between 1.5 and 2 hours. However, during the
 189 ADD process, the inner balloon of the dual-mode balloon is exposed to low temperatures, intense ultraviolet
 190 radiation, and high ozone concentrations for several hours or even up to ten hours. To address these challenges,
 191 the ADDRIS research team conducted formulation tests to enhance the inner balloon resistance to these
 192 environmental factors, with a particular emphasis on natural latex modification, cold resistance, and anti-aging
 193 systems. Considering that latex hot air aging performance improves air tightness and balloons are exposed to
 194 prolonged sun exposure and hydrogen loss, the incorporation of a specific latex compound was found to
 195 augment durability. Fig. 3a and 3b show that the addition of latex formulas had minimal impact on the latex
 196 viscosity and the balloon appearance while improving its tensile strength and thermal aging resistance. Fig. 3c
 197 and 3d demonstrate that butyl oleate exhibits the lowest reduction in low-temperature burst performance after
 198 water extraction and accelerated aging, making it the best-performing cold-resistant agent. Consequently, this
 199 agent was integrated into the formula to bolster cold resistance. For the anti-aging system, illustrated in Fig. 3e
 200 and 3f, nano zinc oxide, which can be diluted directly with water to replace traditional zinc oxide, was used.
 201 Additionally, we incorporated antioxidants to enhance the balloons' resistance against ultraviolet and ozone
 202 degradation. These formula improvements extend the inner balloon lifespan under harsh conditions of low
 203 temperature, intense UV radiation, and high ozone levels. This enhanced durability has been applied to the inner
 204 balloon, resulting in an extended service life and a high success rate during the drift phase (Zhu et al., 2021;
 205 Shen et al., 2020).

206



207



208

209

210

211

212

213

214

215

216

217

218

219

Figure 3. Modification test of natural latex in the inner sphere: (a) Four types of modified natural latex materials—Butyl latex, Japanese chloroprene latex, Chinese chloroprene latex, and Nitrile latex—were screened and added to natural latex using the homogenization method. (b) Physical properties of the modified natural latex pellet samples were evaluated for operational and thermal aging tensile testing. (c) Butyl oleate, Plant polyol, DiOctyl Phthalate (DOP), DiOctyl Sebacate (DOS), DiOctyl Adipate (DOA), and mechanical oil were added to natural latex as cold resistance agents. Cold resistance system test: The blasting diameters of six types of cold-resistant samples were tested using low-temperature blasting instruments at -85°C. (d) Low-temperature blasting diameters were measured for six types of raw, water-pumped, and aged samples with seven parts of cold-resistant agents added. Anti-aging system test: (e) Comparison of tensile properties among nine anti-aging agents—UV327, UV400, UV531, UV1164, and TiO2 filler—with 0.2 parts of one-component anti-aging agent after eight hours of operational and ultraviolet aging. (f) Comparison of tensile properties after ozone aging between Nano ZnO and ZnO.

220

3.2. Payload technology

221

3.2.1 Specialized SoC module of meteorological-sounding

222

223

224

225

226

227

228

229

230

231

The ADDRS payload is similar to operational radiosondes and consists of three main components: positioning systems, PTU (Pressure, Temperature, and Humidity) sensors, and communication modules. It calculates and outputs satellite positioning information and performs real-time monitoring and transmission of meteorological data, including temperature, relative humidity, and pressure. Unlike operational radiosondes, ADDRS operates effectively across all three phases of the ADD process, requiring a minimum operational time of six hours. This extended operation necessitates a larger-capacity battery for the ADDRS radiosonde. Additionally, the radiosonde's weight affects the balloon's inflation volume, making it essential to reduce the radiosonde's weight where possible. Therefore, an integrated, lightweight, and low-power radiosonde is crucial, and the ADDRS research team developed a specialized SoC (System on Chip) module (named Equinox I) for CMA's GTH type of Beidou navigation radiosonde.

232

3.2.2 Highly integrated radiosonde

233

234

235

236

237

238

239

240

241

242

The Tianjin Huayuntianyi Special Meteorological Sounding Tech. Co., Ltd. HT-GTS(U)2-1 (GTH3), which employs a specialized SoC module of meteorological sounding and utilizes a multi-layer board design and miniaturized components to reduce the size, weight, and power consumption. Table 3 demonstrates that the GTH3 radiosonde is significantly better than GTS1 radiosonde (Chinese operational radiosonde before 2025) in volume, weight, and transmission power, with advantages in operational duration and communication rate. The GTH3 participated in WMO UAI2022 (Upper-Air Instrument Intercomparison Campaign organized by the World Meteorological Organization (WMO) and co-organized by the Deutscher Wetterdienst (DWD) in 2022) with the results shown in Table 4. It is suitable for applications in ORUC (Operational and Research Use in Climatology), including aeronautic meteorology, near/ultra-short-term forecasting, global numerical weather prediction, and real-time monitoring (WMO IOM-143., 2024).

Table 3. Comparison of parameters among RS41, GTH3 and GTS1 radiosonde.

Radiosonde type	Positioning method	Volume (mm ³)	Weight (g)	Transmitting power (mW)	Working time (min)	Data Transmission Rate(bps)	Battery Weight (g)	Foam Packaging Weight (g)	Circuit boards Weight (g)
GTS1 radiosonde	Radar positioning	190×90×245	<400	400≤	>120	1200	<250	<70	<80
GTH3	Equinox I	155×65×60	<120(for one profile)	100≤	>240	Optional,2400,4800,9600	<40	<30	<50
		155×65×60	<170(for “ADD” three phase profile)	100≤	>640		<90	<30	<50

Vaisala RS41

	u-blox G7020	155×60×46	109	60	>240	4800	76	/	/
--	--------------	-----------	-----	----	------	------	----	---	---

244 Table 4. The evaluation results of GTH3 radiosonde temperature, pressure, relative humidity, wind and geopotential height in WMO Instruments and Observation Methods Report
245 No. 143, page.150(Note: The data are in the form of $\Lambda_{c,L} \delta_{c,L} \pm \epsilon_{c,L}$, where $\Lambda_{c,L}$ represents the individual measurement root mean square error, $\epsilon_{c,L}$ denotes the measurement
246 uncertainty, $\delta_{c,L}$ is the measurement error, and $\sigma(\delta)$ indicates the measurement standard deviation. The planetary boundary layer (PBL) ranges from surface to 2 kilometers; the
247 free troposphere (FT) ranges from 2 kilometers to the tropopause 12 kilometers are in the ; the upper troposphere/lower stratosphere (UTLS) ranges from 7 kilometers to 17
248 kilometers; the middle and upper stratosphere (MUS) is above 17 kilometers up to the bursting point of the sounding balloon.)

Time	Height	Atmospheric temperature [K]	Relative humidity [%RH]	Geopotential height [m]	Pressure [hPa]	Wind (horizontal)direction[°]	Wind (horizontal)speed [ms ⁻¹]	Wind (horizontal)vector [ms ⁻¹]
Day	PBL	$0.18_{0.17}^{-0.05} \pm 0.03$	$7.00_{4.41}^{-5.43} \pm 0.74$	X	X	X	X	X
	FT	$0.12_{0.11}^{+0.05} \pm 0.04$	$8.75_{8.02}^{-3.50} \pm 0.60$	$5.9_{5.5}^{+2.0} \pm 1.8$	$0.4_{0.4}^{-0.0} \pm 0.1$	$3.6_{3.6}^{-0.4} \pm 0.2$	$0.2_{0.2}^{-0.0} \pm 0.0$	$0.3_{0.1}^{+0.2} \pm 0.0$
	UTLS	$0.09_{0.08}^{+0.01} \pm 0.03$	$7.73_{7.58}^{-1.55} \pm 0.40$	$13.2_{8.6}^{+10.0} \pm 3.8$	$0.4_{0.2}^{-0.3} \pm 0.1$	$2.5_{2.5}^{-0.2} \pm 0.3$	$0.2_{0.2}^{-0.0} \pm 0.0$	$0.3_{0.2}^{+0.2} \pm 0.0$
	MUS	$0.27_{0.16}^{-0.22} \pm 0.10$	$1.69_{0.82}^{+1.48} \pm 0.46$	$29.5_{17.9}^{+23.4} \pm 4.2$	$0.3_{0.1}^{-0.2} \pm 0.0$	$6.1_{6.1}^{-0.4} \pm 0.2$	$1.3_{1.3}^{-0.0} \pm 0.0$	$1.5_{1.5}^{+0.3} \pm 0.0$
Night	PBL	$0.38_{0.34}^{-0.18} \pm 0.05$	$4.72_{4.66}^{+0.74} \pm 0.15$	X	X	X	X	X
	FT	$0.15_{0.15}^{+0.02} \pm 0.02$	$6.41_{6.03}^{+2.16} \pm 0.11$	$5.8_{5.8}^{+0.4} \pm 0.4$	$0.5_{0.5}^{+0.1} \pm 0.2$	$2.6_{2.6}^{-0.2} \pm 0.2$	$0.2_{0.2}^{-0.0} \pm 0.0$	$0.2_{0.1}^{+0.2} \pm 0.0$
	UTLS	$0.12_{0.10}^{+0.06} \pm 0.05$	$6.82_{5.74}^{+3.70} \pm 0.26$	$11.5_{8.6}^{+7.7} \pm 3.4$	$0.3_{0.2}^{-0.1} \pm 0.1$	$2.4_{2.4}^{-0.1} \pm 0.1$	$0.2_{0.2}^{+0.0} \pm 0.0$	$0.2_{0.1}^{+0.2} \pm 0.0$
	MUS	$0.10_{0.10}^{-0.03} \pm 0.02$	$1.71_{0.74}^{+1.54} \pm 0.28$	$26.7_{16.8}^{+20.7} \pm 4.2$	$0.1_{0.1}^{-0.1} \pm 0.0$	$4.5_{4.4}^{-0.6} \pm 0.2$	$0.2_{0.2}^{-0.0} \pm 0.0$	$0.4_{0.3}^{+0.3} \pm 0.0$

251 3.2.3 Drifting controller

252 The drifting controller can be considered part of the ADDRS payload. It connects to an inner balloon above
253 and a parachute and radiosonde below. The controller fuses a wire with an instant high electric current,
254 triggering the mechanical device to disconnect the parachute and the radiosonde. The controller serves two main
255 functions during the drift phase:

- 256 1. Reduce the weight of the sounding equipment by releasing a pre-carried counterweight, in order to adjust
257 the gravity or altitude of the inner balloon and its load during the drift phase.
- 258 2. Separate the inner balloon from the other sounding equipment (parachute and radiosonde). Moreover, the
259 drifting controller can also initiate the fuse based on predetermined control rules, such as altitude limits
260 (≤ 18 km), specified time, the latitude and longitude of a designated area, or upon receiving commands
261 from the ground. This action can be taken before the drifting balloon is about to enter the specified area or
262 approach the maximum drift height. As a result, it will effectively end the drift phase, separating the
263 parachute and radiosonde from the balloon.

264 3.3. Receiving radiosonde data and sending control instructions technology

265 The ADDRS ground data-receiver utilizes a high-gain, low-power, ultra-compact omnidirectional antenna,
266 along with super-heterodyne architecture and multiple communication protocol algorithms, including time
267 division multiple access, frequency division multiple access, and code division multiple access (Gong et al.,
268 2021). It supports various frequency modulation modes and achieves a receiving sensitivity of better than -120
269 dBm (at 2400 bps), effectively addressing self-interference issues in multi-channel radiosonde data reception.
270 Additionally, the system incorporates narrow-band wireless communication technology to improve low-
271 elevation reception when the radiosonde drops below the receiving antenna's height, facilitating broad-area
272 coverage with a visual range radius for upper-air coverage of at least 200 km. The receiver can adapt to diverse
273 application scenarios, such as fixed stations, vehicles, and ships. With an average data reception rate of 99.7%,
274 the ground receiver at the Anqing station has demonstrated an impressive maximum reception distance of up to
275 487 km.

276 Unlike the one-way (downlink) communication mode used in operational sounding systems, the ADDRS
277 control command transmitter can send ground instructions to the drifting controller, with a linear
278 communication range extending beyond 300 km. This capability allows for precise control over the drifting
279 controller to execute actions such as releasing counterweights or separating the balloon from the parachute and
280 radiosonde, enabling the radiosonde to conduct drift phase measurements within the target area (Liu et al., 2021).
281 During field tests, over ten balloon discharge control commands were successfully transmitted, with the farthest
282 reaching 403 km.

283 3.4. "ADD" measurement technology

284 The details of the ADD measurement method are outlined by (Cao et al., 2019). The ascent phase
285 measurement technique adheres to the guidelines outlined in the Guide to Operational Upper-Air Meteorological
286 Observation. The primary research focus of the ADDRS is on the measurement techniques for the drift and
287 descent phases.

288 **3.4.1 Temperature measurement method in the flat drift phase**

289 During the drift phase of ADDRS, the inner sphere of the dual-mode balloon moves with the horizontal
290 airflow in the stratosphere. The radiosonde's vertical movement, with the surrounding atmosphere, is minimal
291 and can be approximately considered as drifting with the horizontal wind. The effect of radiation on the
292 temperature sensor during this phase is significantly greater than during the ascent and descent phases, leading
293 to considerable measurement errors that are challenging to correct using general quality control algorithms. For
294 instance, Vaisala RS41 radiosonde software often flags such data as invalid in operational radiosonde
295 observations.

296 Given the unique conditions of stratospheric air temperature measurement, the ADDRS research team
297 employs a multi-physical field, fluid-structure coupled computational fluid dynamics (CFD) approach to model
298 the behavior of the temperature sensor in high-altitude, low-wind-speed environments. This model calculates the
299 flow and the temperature field, accounting for radiation effects based on sun elevation, ventilation, sensor size,
300 and surface reflectivity. To ensure broad applicability, neural networks, and other mathematical methods are
301 used to fit the extensive simulation data, yielding practical error-correction equations (Yang et al., 2014).

302 Considering that there may be discrepancies between CFD simulations and real environmental conditions,
303 the ADDRS research team uses instruments such as low-pressure wind tunnels and solar simulators to create an
304 experimental platform. This setup simulates ventilation, air density, and solar radiation conditions during the
305 drift phase, allowing for the measurement of temperature errors due to solar radiation. These measurements
306 verify and refine the simulation-based error correction equations (Yang et al., 2022).

307 **3.4.2 Vertical wind data extracted by parachute landing**

308 Currently, due to the pendulum effect, vertical wind measurements cannot be performed in balloon-borne
309 soundings. The parachute-drop wind measurement model established by the WMO and NCAR does not address
310 vertical wind measurement directly (Wang et al., 2015), instead assuming a zero vertical wind speed. This
311 model assumes that the parachute-drop system is influenced only by gravity and vertical resistance, omitting
312 other factors like buoyancy, additional forces, and parachute rotation during descent. This limitation prevents
313 the analysis of vertical wind and also affects the accuracy of horizontal wind field calculations (Jensen et al.,
314 2010; Ingleby et al., 2022).

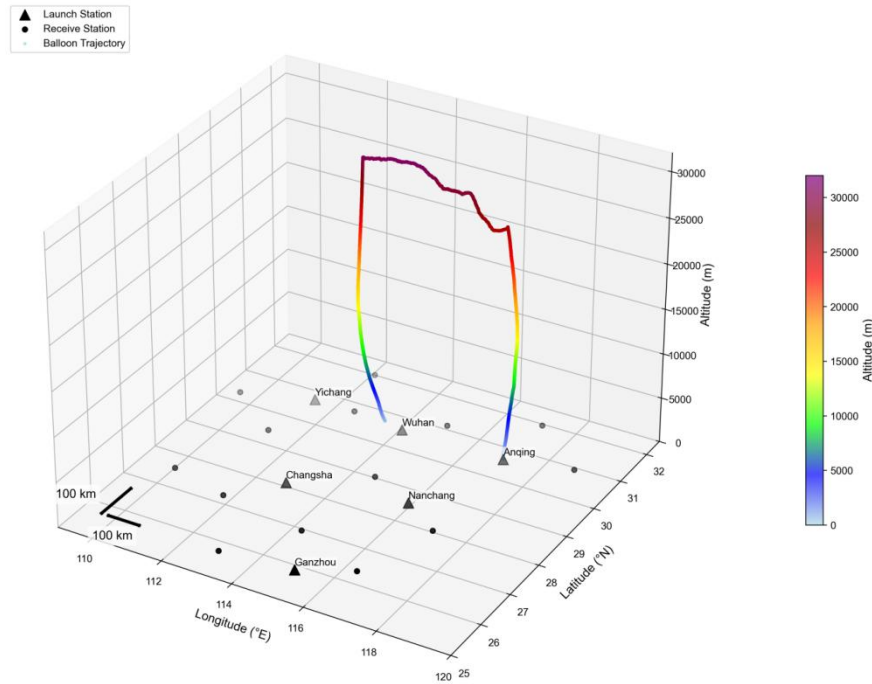
315 Therefore, the ADDRS research team developed a more comprehensive vertical wind measurement model
316 by considering all relevant forces acting on the parachute descent system (Guo et al., 2018). Comparative tests
317 led to the selection of conical parachutes to minimize swing effects on measurements, with the parachute area
318 tailored to match the radiosonde weight. As a result, ADDRS achieves a stable descent speed of approximately 6
319 m/s \pm 1 m/s, a swing angle below 5°, and a vertical wind measurement uncertainty of less than 1 m/s. These
320 findings demonstrate that the model is effective for calculating vertical wind.

321 **4. Field experiments and data quality verification**

322 **4.1. Field experiment in the middle and lower reaches of the Yangtze River Region**

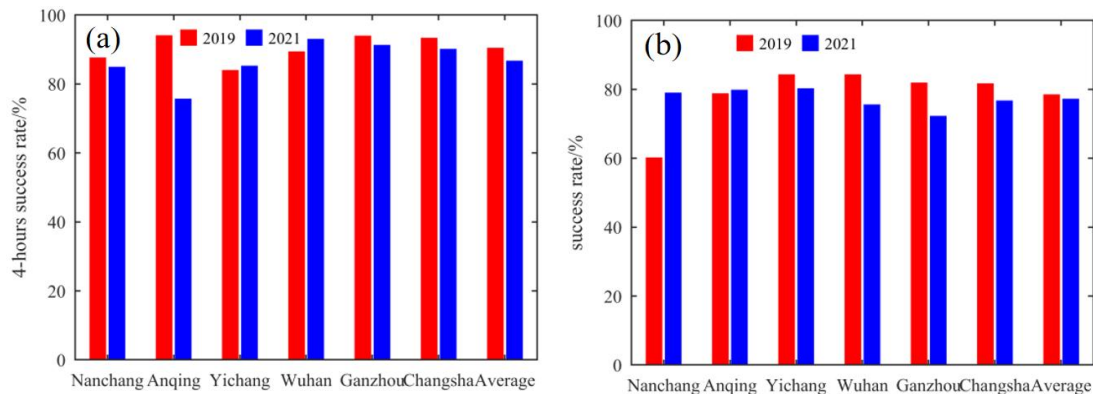
323 From 2019 to 2021, ADDRS conducted field tests and application research across a wide area in the middle
324 and lower reaches of the Yangtze River in China. The research focused on measurement data processing

325 methods, quality control algorithms, and application technologies across diverse scenarios. The ADDRS
 326 network spans six stations: Anqing, Wuhan, Yichang, Nanchang, Changsha, and Ganzhou, located in Anhui,
 327 Hubei, Jiangxi, and Hunan provinces. A total of 14 ground radiosonde data receivers were strategically
 328 positioned around these six stations, spaced approximately 150 km apart. The test covered an area of 600,000
 329 square kilometers, as shown in Fig. 4, and show a trajectory for ADDRS at the Anqing station at 12:00 UTC on
 330 11 July 2021.



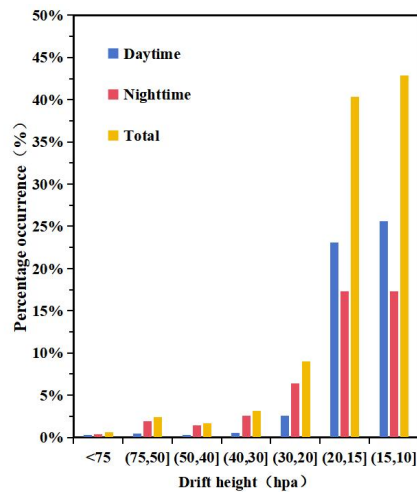
331
 332 **Figure 4. The network distribution of ADDRS and an example of measurement: the trajectory for ADDRS at the**
 333 **Anqing station at 12:00 UTC on 11 July 2021. The black triangles represent balloon launch stations of ADDRS , while**
 334 **the black dots represent receive radiosonde data stations of ADDRS.**

335 During the 13-month experimental period, 3,177 ADDRS launches were conducted, with 3,012 classified
 336 as effective launches, of which 2,369 achieved successful drifting. Among these, 2,136 launches resulted in
 337 drifting for more than 4 hours. The overall drifting success rate was 78.65%, with a 4-hour drifting success rate
 338 of 70.91% (Fig. 5).
 339



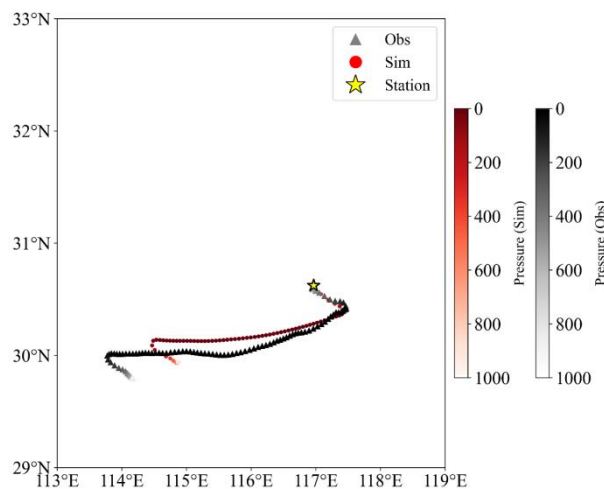
340
 341 **Figure 5. The field experiment in the middle and lower reaches of the Yangtze River Region (2019-2021): (a) Drifting**
 342 **success rate; (b) 4-hour drifting success rate.**

343 From March to September 2021, 2,427 “ADD” radiosonde launches were conducted, with 2,281 classified
 344 as effective launches, of which 1,772 achieved successful drifting. Among these, 1587 launches resulted in
 345 drifting for more than 4 hours. The overall drifting success rate was 77.68%, with a 4-hour drifting success rate
 346 of 69.57%. The 1,772 successful drifts were analyzed (Fig. 6), and 937 were successful during the daytime,
 347 accounting for 52.88%. The successful nighttime drifting was 835 times, accounting for 47.12%, and the effect
 348 of daytime was better than nighttime. The drift heights ranging from < 75hPa (<18km) to 15hPa-10hPa (28km-
 349 32km) were statistically analyzed. The proportion of outer ball explosion heights within 15hPa-10hPa (28km-
 350 32km) was the largest (42.89%). And the proportion of 20hPa-15hPa (26km-28km) is 40.35%, the proportion of
 351 30hPa-20hPa (24km-26km) is 8.97%, and the total proportion of beyond 30hPa is 92.21%. Therefore, the drift
 352 height should basically meet the 30hPa requirement of GBON (WMO, 2020).



353
 354 **Figure 6. The sounding-forecasting interactive network experiment (2021): (a) drifting height; (b) descent height.**

355 Due to the limited availability of high frequency, continuous measurement data for the stratospheric
 356 atmosphere, experiments were conducted in the middle and lower reaches of the Yangtze River to obtain direct
 357 measurement data with high spatial and temporal density (Zhang et al., 2021). The simulated and observed
 358 trajectories are represented by red and black, respectively (Fig. 7). A color gradient based on pressure altitude is
 359 used to indicate the variation of trajectory height along the path.



360
 361 **Figure 7. Observation (black triangles) and simulation (red dots) trajectory diagram. The yellow pentagrams**
 362 **represent radiosonde observations stations, and the colour of the dots represent the corresponding pressure heights.**

363 **The colour range from light to dark, indicating the process of the trajectory rising from low altitude (high pressure)**
 364 **to high altitude (low pressure).**

365 The balloons drifting of ADDRS radiosondes data in stratosphere have been very useful for verification
 366 FY-3D satellite temperature and humidity profiles (Zhou et al., 2023; Zhou et al., 2024). And application in
 367 observing certain features of gravity waves in the lower stratosphere (He et al., 2024; Yang et al., 2021) and
 368 feature extraction and analysis of atmospheric turbulence (Yang et al., 2023).

369 **4.2 Data quality evaluation**

370 Aiming at the characteristics of high-resolution ADDRS data for quantitative application, the ADDRS
 371 research team carefully evaluated ADDRS data using 31 data quality control methods based on the guidelines
 372 for operational upper-air meteorological observation (Wang, D et al. 2020). For the data quality of the ascent
 373 phase of the ADD radiosonde, refer to the results in Table 4. Additionally, the fifth generation of ECMWF
 374 (ERA5) global reanalysis (Hersbach et al., 2020) was used to evaluate the quality of four upper-air radiosonde
 375 observations stations' ADDRS data in Guangdong in August 2022in (Zhang, C.Z et al., 2025), and Table 5
 376 shows the results of field experiment in the middle and lower reaches of the Yangtze River Region (2019-2021).
 377 Compared with the data in the ascent phase and the descent phase, the results for temperature, u-wind, v-wind,
 378 and the standard deviation of geopotential height show good consistency, relative humidity shows weaker
 379 uniformity. The conclusion is basically consistent with the results of Table 4 in the section 3.2.2.

380 **Table 5. Comparative analysis of after-quality control of ADDRS radiosonde data and ERA5.**

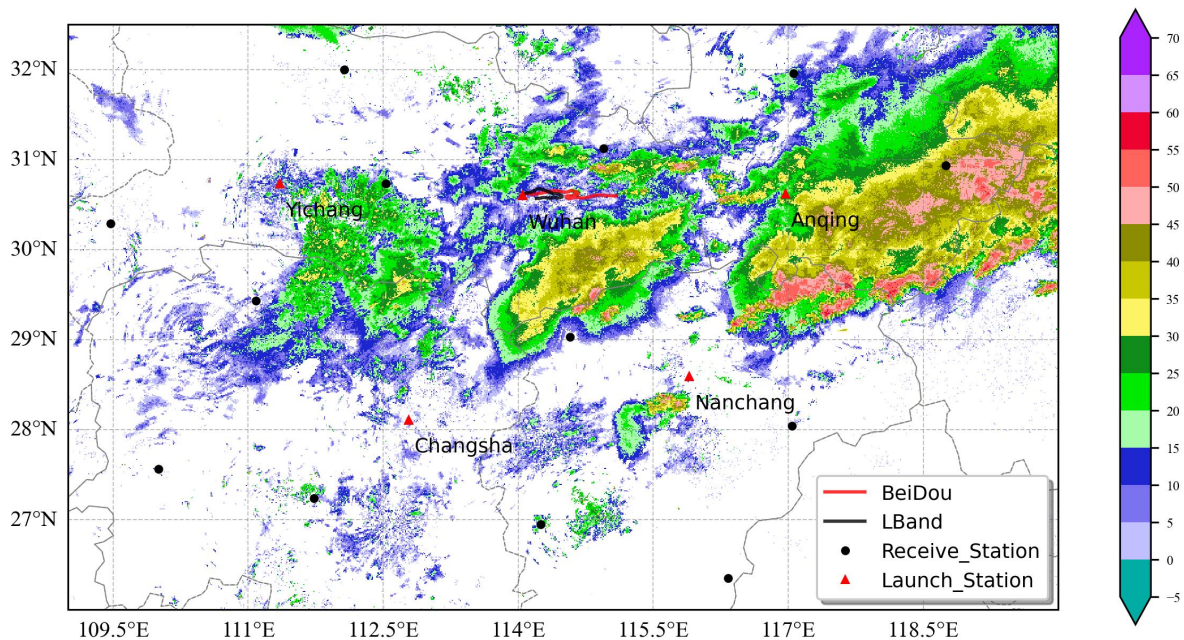
			U (m/s)		V (m/s)		T (K)		RH (% RH)	
			bias	std	bias	std	bias	std	bias	std
Ascent	Day	Above tropopause	0.03	1.73	0.11	1.91	-0.4	1.04	/	/
		Below tropopause	0.13	1.41	0.08	1.47	0.04	0.69	1.32	8.57
	Night	Above tropopause	-0.02	1.72	-0.01	1.87	0.01	1.02	/	/
		Below tropopause	0.13	1.4	0.02	1.46	0.08	0.66	1.62	8.32
Drift		above tropopause	/	3.32	/	3.22	/	3.09	/	/
Descent	Day	Above tropopause	0.16	1.74	-0.02	1.9	0.9	1.14	/	/
		Below tropopause	0.14	1.65	0.01	1.7	0.42	0.75	-1.7	10.12
	Night	Above tropopause	0.16	1.73	0.03	1.84	0.21	1.06	/	/
		Below tropopause	0.15	1.67	0.05	1.67	0.04	0.73	0.5	10.47

381 **5. Application of ADDRS in numerical forecasting techniques**

382 **5.1 The applications in weather analysis**

383 Through long-term testing, the ADDRS have the potential for capture key information in convective
 384 system monitoring. From July 8 to 9, 2021, a strong convective weather event with a long duration and a large
 385 impact area occurred in the middle and lower reaches of the Yangtze River in China. Convection developed and
 386 moved to northern Jiangxi, northern Zhejiang, southern Anhui, and southern Jiangsu overnight on July 8 (Fig.8).
 387 The drifting trajectories of ADDRS radiosondes were from west to east, which aligned with the movement and

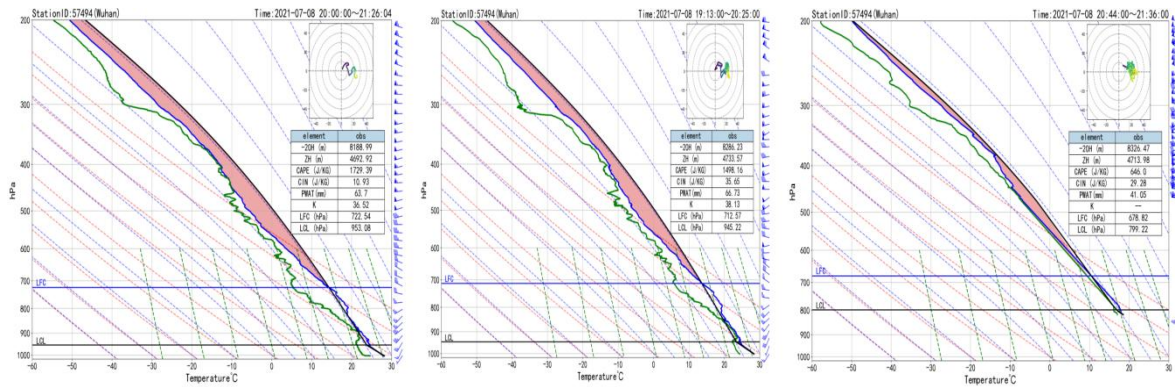
388 development direction of severe convection. The descent phase radiosondes of ADDRS provides effective
 389 monitoring and significant insights in track the occurrence of the convective system and the changes in the
 390 ambient field.



391
 392 **Figure.8 The trajectory for Beidou radiosonde and LBand(GTS1) radiosonde at the Wuhan station and radar**
 393 **reflectivity image at 12:00 UTC on 11 July 2021.**

394 Fig.8 presents the trajectory data for both the ADDRS(Beidou) radiosonde and the GTS1(LBand
 395 radiosonde), which were recorded at the Wuhan meteorological station. At 19:15 on the night of the 8th, Wuhan
 396 was located on the west side of the main body of the convection, and the ADDRS radiosonde was launched
 397 from the Wuhan station. Subsequently, at 20:00, the GTS1 radiosonde was also deployed from the same location.
 398 The trend of the ADDRS radiosonde curve in the ascent phase (Fig. 9b) mirrored the trend observed for the
 399 GTS1 radiosonde (Fig. 9a). It was evident from the radiosondes in the ascent phase that the CAPE values of the
 400 ADDRS radiosonde and GTS1 radiosondes differed with the development of convection. The CAPE value of
 401 the GTS1 at 20:00 was 1729.39 J/kg, exceeding the 1498.16 J/kg detected by ADDRS radiosonde at 19:15.
 402 Influenced by an upper-level westerly jet, the ADDRS sounding balloon drifted eastward toward the Wuhan. At
 403 21:30, ADDRS conducted descent phase measurements (Fig. 9c). As shown in the layer curve, the CAPE value
 404 at 21:30 decreased significantly compared with that at 20:00, dropping to 646.0J/kg, which was lower than the
 405 energy recorded at the Wuhan station. There is still a westerly jet stream with wind speed greater than 20m/s
 406 beyond the upper-air of 500hPa level. The east of Wuhan proximity to the main body of convection, the
 407 reduction in energy suggests intensive of upward motion, leading to the reduction of effective potential energy
 408 and further develop of convective. Notably, the GTS1 radiosonde, launched from Wuhan, ceased data collection
 409 after the ascent phase, thus missing this crucial change. The descent phase of ADDRS demonstrates
 410 robust monitoring capabilities and holds significant implications, as it can timely captures environmental
 411 conditions favorable for convection onset and development, including wind patterns, effective potential energy,

412 and humidity at downstream locations.. These findings enable researchers to analyze changes in the upper-air
413 field and the occurrence of catastrophic weather convective systems.



414

415 **Figure 9. Comparison of ADDRS and GTS1 radiosonde T-logP at the Wuhan station: (a) GTS1 radiosonde; (b)**
416 **ascent phase of ADDRS radiosonde; (c) descent phase of ADDRS radiosonde.**

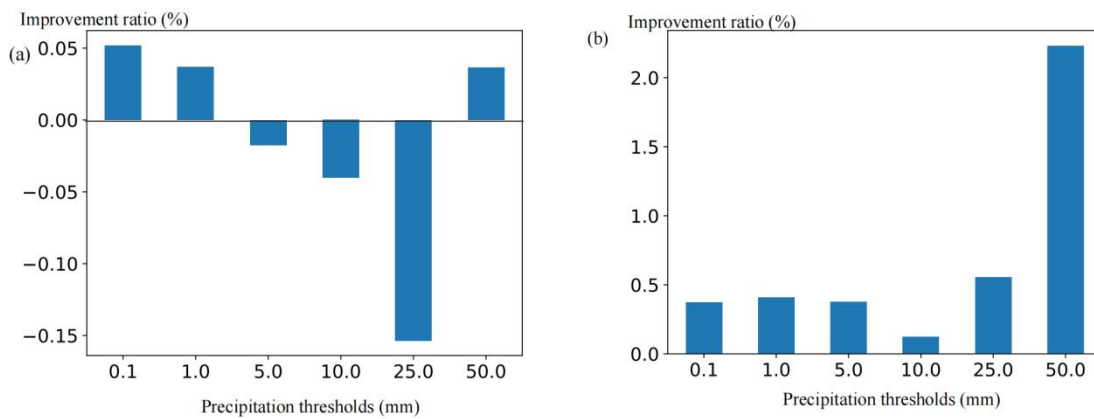
417 5.2 Applications in numerical weather prediction (NWP)

418 Compared with GTS1 radiosondes, the ADDRS radiosondes of ascent and descent phase measurement data
419 for numerical weather prediction (NWP), achieving a similar role to intensive sounding and providing more
420 continuous, direct stratospheric measurement data (Zhang, X et al., 2025; Zhang, X.P et al. 2023). The
421 Numerical Department of the China Meteorological Administration developed the key technology for ADDRS
422 assimilation in the CMA-MESO 3DVar (three-dimensional variational mesoscale) (Zhuang et al. 2019) and
423 CMA-GFS 4DVar systems (four-dimensional Variational Global Forecast System) (Wang, R. W et al., 2021).
424 To avoid the tangent linear and adjoint models, the four-dimensional ensemble forecast error is introduced into
425 the CMA global data assimilation system, and the Hybrid-4DEnVar assimilation scheme is developed. The
426 batch cycling forecast experiments and typhoon forecast experiments are conducted and compared with the
427 4DVar scheme (Gong et al., 2019; Wang, F et al., 2024). Specifically, this includes observation operators that
428 consider drift positions and vertical sparring methods, such as selecting the nearest radiosonde data from the
429 model layer for assimilation. We employed the CMA-MESO system to conduct a measurement data
430 assimilation in the ADDRS descent phase across six test stations in the middle and lower reaches of the Yangtze
431 River from July 1 to July 31, 2021. We set up the control test (CTL) as in the CMA-MESO system, and the
432 observed data included traditional sounding data, ground reports, aircraft reports, cloud-guided wind, radar
433 radial wind, GNSS occultation refractive index, and ground-based GNSS retrieval of the atmospheric whole-
434 layer precipitation water. ADDRS data assimilation was added to the control CTL in the Down test.

435 The impact of the ADDRS descent phase measurement data on the precipitation forecast at CMA-MESO at
436 03, 06, 09, 15, 18, and 21 UTC (termed the warm start times) was evaluated. Compared to the TS (Threat Score),
437 the ETS (Equitable Threat Score) imposes stricter penalty for false alarms and missed reports, making the
438 scoring more equitable. The results of the one-month batch test indicate that assimilating ADDRS descent phase
439 data improves precipitation forecasting skills, especially for heavy precipitation above a certain magnitude. Fig.
440 10a and Fig. 10b illustrate the improvement rates in accumulated precipitation forecasting skills for the 0-12
441 hour and 12-24 hour periods from the warm start time. Positive values indicate that the precipitation forecasting
442 skills of the Down test are improved compared with those of the CTL test, while negative values indicate a

443 decrease in forecasting skills for the Down test. The ETS scores for precipitation forecasts in the 0-12 hour
 444 range at thresholds of 0.1 mm, 1 mm, and 50 mm increased slightly, averaging about 0.04% (Fig. 10a). Due to
 445 the timeliness required for forecasting, the 12-24 hour precipitation forecast is of particular interest to
 446 forecasters. As illustrated in Fig. 10b, the Down test demonstrated enhanced ETS scores for precipitation
 447 forecasts across all levels within the 12-24 hour range, with an average increase of 0.7% at the 50 mm
 448 threshold and a notable 2.2% improvement specifically at this level .

449 In addition, we utilized CMA-MESO V5.1 to conduct Observing System Simulation Experiments (OSSE)
 450 under the ADDRS network nationwide. The results indicate that once the ADDRS network observation is
 451 implemented, the national precipitation forecast skills of the CMA-MESO fast cycle assimilation forecast
 452 system at warm startup time can improve by 2%-5%. The potential operational applications of ADDRS high-
 453 resolution data were quantitatively evaluated using a numerical model (Wang, R. W et al., 2023). After the
 454 application of ADDRS data in CMA-GFS 4DVar assimilation, the temperature analysis error at 06:00 and 18:00
 455 was reduced by more than 2% and the average prediction skill of the CMA-MESO accumulated precipitation
 456 results for the 12-36 hour period improved by 1% (Wang, J. C. et al., 2024).



457
 458 **Figure 10. Improvement rates of cumulative precipitation thresholds (mm) predictions for 0-12 hours (a) and 12-24**
 459 **hours (b) in the Down test compared to the control test.**

460 5.3 Applications in targeted observations

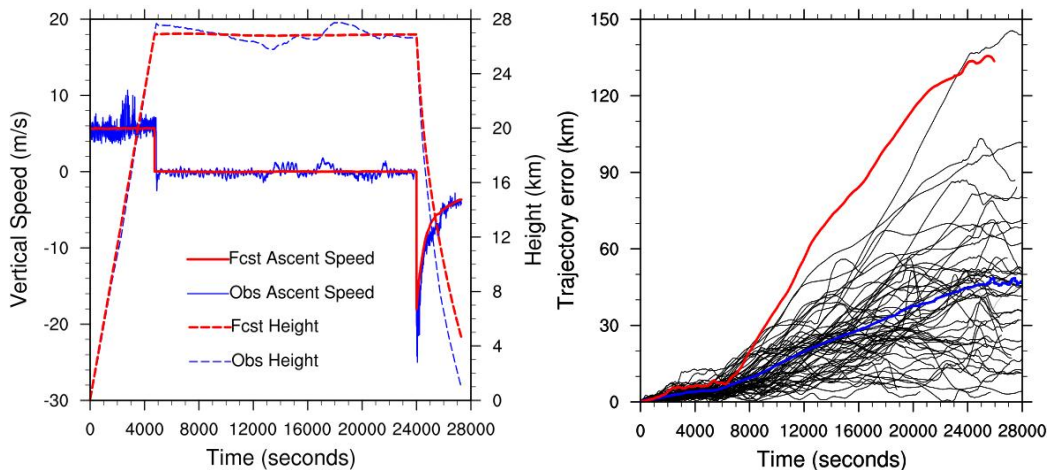
461 Targeted observation have sometimes been one of frontier field in atmospheric science research. They
 462 represent an important method to address the shortcomings of operational observation systems in monitoring
 463 extreme weather events. Furthermore, they significantly enhance the initial field quality and forecast accuracy of
 464 numerical models, which is crucial for predicting extreme weather disasters (Majumdar., 2016). With its
 465 capacity for “ADD” measurement, the ADDRS has the potential to conduct targeted observations in uninhabited
 466 areas, rarely observed regions, and during specific extreme weather events. However, since the ADDRS lacks a
 467 power system, accurate trajectory prediction is essential for utilizing the descent phase for vertical
 468 measurements in these locations. This requires careful consideration of appropriate drift height, launch time, and
 469 launch location, allowing the ADDRS sounding to be carried to the target observation area by the ambient wind
 470 field.

471 In this context, a trajectory prediction and selection method based on high-resolution numerical weather
 472 prediction technology has been proposed for ADDRS (Wang, J. C et al., 2021). Additionally, Majumdar (2016)

473 highlights that advancements in numerical weather prediction (NWP) systems—such as improved data
 474 assimilation techniques and enhanced model resolution—have reduced the marginal contributions of individual
 475 observing systems. Furthermore, the evaluation of targeted observations is constrained by factors including
 476 flow-dependent conditions, limited sample sizes, and inconsistencies in verification metrics. Therefore, cost-
 477 effective strategies for targeted observations necessitate exploration through multi-agency coordinated
 478 observing system experiments, such as FSO studies (Magnusson et al., 2025).

479 5.3.1 Trajectory prediction method and software system

480 The issues of low temporal resolution and prediction accuracy associated with the linear extrapolation
 481 method used in balloon trajectory prediction (Brown et al., 2024). The balloon trajectory equation is directly
 482 embedded into a high-resolution numerical weather model system that utilizes a model atmospheric
 483 environment with high temporal resolution (1-10 seconds) and high spatial resolution (1-3 km). This approach
 484 enables precise simulation of vertical velocity during the ADDRS descent phase (Fig. 11a), significantly
 485 enhancing the accuracy of ADDRS trajectory prediction and the simulation of descent velocity. The average
 486 prediction error for a 6-hour trajectory is less than 40 km (Fig. 11b).



487

488 **Figure 11. (a) Comparison of simulated (red line) and observed (blue line) vertical speeds of ADDRS radiosonde data**
 489 **during the descent phase at the Anqing station at 11:17 on June 20, 2018; (b) Deviations of 63 pairs of simulated**
 490 **ADDRS trajectories versus observed trajectories (black line), with the average deviation indicated by the blue line**
 491 **and the largest forecast deviation shown by the red line.**

492 5.3.2 Trajectory selection method based on the collection idea

493 To observe the ADDRS in the target observation area, we proposed a method of elevation selection based
 494 on ensemble forecasting, considering the characteristics of the atmospheric wind field as it varies with altitude.
 495 The main idea of this method is to predict the trajectories of all ADDRS stations at different drifting heights and
 496 select the heights closest to the target observation area. The details are as follows:

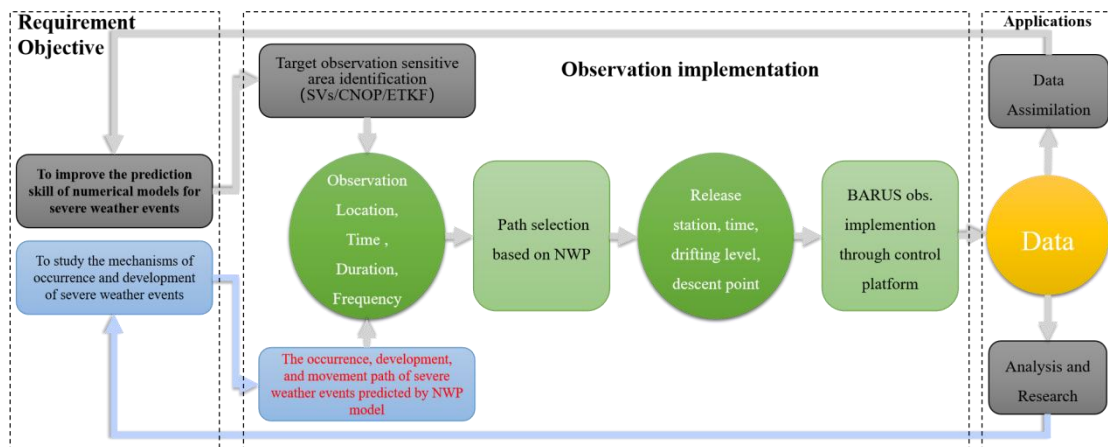
- 497 1. Identify the positions and launch time: Given the positions $S_m(x_m, y_m, z_m)$ of M ADDRS launch stations and
 498 the launch time t_r .
- 499 2. Select safe drift heights: Choose N safe drift heights h_1, h_2, \dots, h_n , that comply with civil aviation safety
 500 regulations as flat drift heights.

- 501 3. Trajectory prediction: Utilize the trajectory prediction system to predict the ADDRS trajectories under the
 502 above conditions within 12 hours, resulting in $T_{nm}(x,y,z,t)$ for N trajectories at each of the M launch
 503 stations.
- 504 4. Calculate closest trajectory: From the $M \times N$ trajectories obtained in step 3, calculate the trajectory closest
 505 to the target observation point. When the distance is less than the predetermined standard distance L_C that
 506 can meet the requirements, the releasing ADDRS station and the drifting height H_s are selected, and the
 507 time nearest to the target area is taken as the descent time t_s . If no suitable drift height meets the conditions,
 508 the trajectory selection fails.
- 509 5. Implement target observation: Input the information regarding the ADDRS balloon launch station, drift
 510 height, and descent time determined in step 4 into the ADDRS operation command system to execute the
 511 target observation.

512 **5.3.3 Targeted observations experiment of Typhoon**

513 The ADDRS research team proposed a 'full chain' implementation for target observation using ADDRS
 514 (Fig. 12). This implementation plan, designed to provide technical support for ADDRS applications in disaster
 515 weather monitoring, forecasting, and mechanism research, encompasses three primary stages. Initially, the
 516 requirements for target observation are established. These requirements fall into two categories: one focusing on
 517 specific disaster weather events and the other on sensitive areas to improve future numerical prediction skills.
 518 The target observation area is then determined based on the type of demand. For the first category, the specific
 519 location of anticipated disaster weather is identified through numerical prediction results. For the second
 520 category, the target observation location is determined using CMA-GFS singular vector technology.

521 Subsequently, the trajectory selection system is invoked to ascertain the ADDRS discharge radiosonde
 522 observations station, drift height, discharge time, and other relevant information. This information is then
 523 transmitted to the operation command system of ADDRS to guide the stations in implementing ADDRS
 524 measurements. Ultimately, the ADDRS target observation data is distributed to users for application and
 525 evaluation.

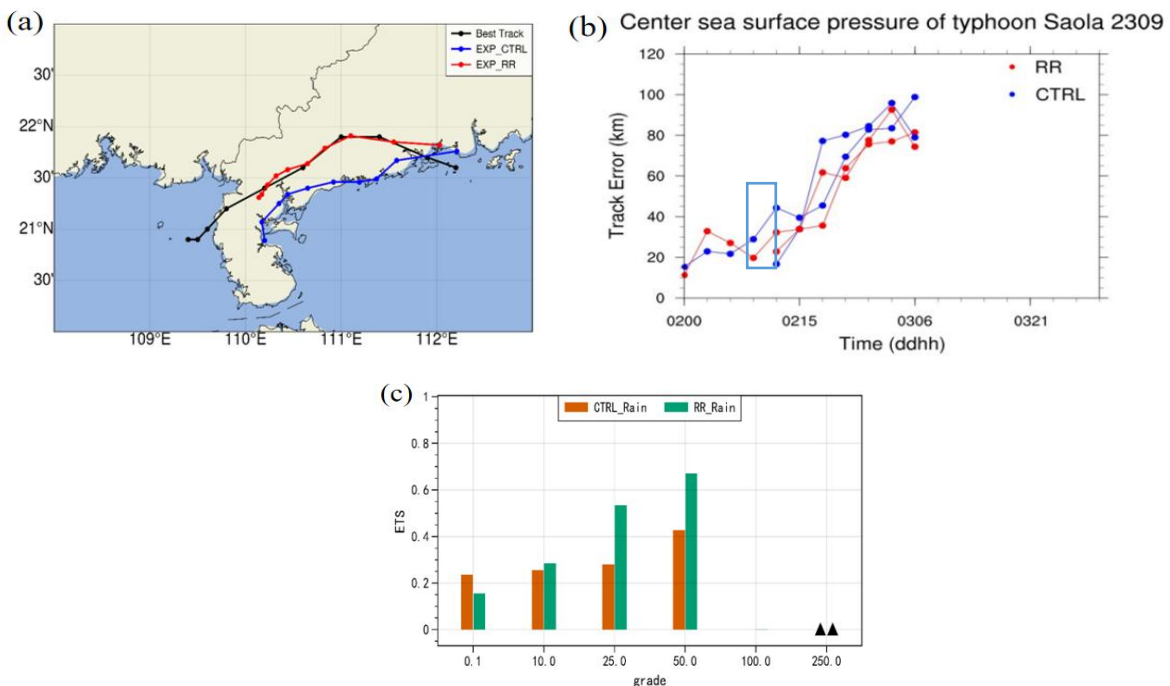


526
 527 **Figure 12. Technical route for targeted observations of typhoons and other severe weather using ADDRS and CMA-**
 528 **MESO models.**

529 According to the implementation plan for ADDRS target observation (Zhang et al., 2021; Liu, L. H et al.,
 530 2022), we made a preliminary attempt to conduct a target observation experiment on Typhoon 2309 'SAOLA'

531 (Lau et al., 2024) formed at 00 UTC on August 28, 2023. By 00 UTC on September 1, it was expected that
 532 'SAOLA' would land near Guangdong on September 2. Therefore, the demand for vertical profile data of the
 533 internal interface of Typhoon 'SAOLA' became imperative. Using the typhoon trajectory predicted by CMA-
 534 GFS, we pinpointed the typhoon's position for 12:00 PM on September 2 post-landfall. The ADDRS trajectory
 535 selection system was then engaged to ascertain the balloon launch station and drift height that could reach or
 536 come closest to the typhoon area, ranging from the minimum navigation safety height of 21 km to 29 km. We
 537 set ten different drift levels at 1 km intervals, with trajectory predictions and simulations conducted from four
 538 radiosonde observations stations in Guangdong. Yangjiang radiosonde observations station in Guangdong was
 539 ultimately chosen for the launch, scheduled for 06:00 on September 2, 2023, with a drift level of 25 km.

540 We calculated the required air capacity for the dual-mode balloon, and the 'ADD' subsystem was prepared
 541 to be deployed by radiosonde observations station personnel. When the radiosonde reached the core area of
 542 'SAOLA,' the radiosonde dispatched commands to the 'SAOLA' controller via control command transmission
 543 equipment, successfully observing the descent section 80 km from the center of Typhoon 'SAOLA.' The
 544 obtained ADDRS data was subsequently assimilated into the CMA_MESO 3DVar system. Late test results
 545 indicated that after assimilating the data from the ADDRS descent phase, the forecast error for the typhoon
 546 trajectory reported since 06:00 on September 2, 2023, was significantly reduced. Specifically, the typhoon
 547 trajectory error at 02:18 was reduced from 62.7 km to 35 km in the control test, marking an improvement of
 548 44.18%. Additionally, precipitation forecasting techniques exhibited significant improvements: from 0.25 to
 549 0.30 in the 10 mm scale, from 0.30 to 0.55 in the 25 mm scale, and from 0.45 to 0.70 in the 50 mm scale. These
 550 results effectively demonstrate the potential of ADDRS in target observation and numerical assimilation
 551 applications (Fig. 13). It is worth noting that the initial use of ADDRS for target observation served as a
 552 foundational attempt, paving the way for future ADDRS operations and maximizing its utility (Wen., et al.,
 553 2024).



554

555

556 **Figure 13. 2023-09-02 UTC 00-12h: (a) Control test (blue), ADDRS data assimilation impact test (red), and optimal**
 557 **trajectory of Typhoon 'Saola' (black); (b) Comparison of sea level pressure at the central point of Typhoon 'Saola'**

558 between the control test (blue) and the ADDRS data assimilation impact test (red); (c) ETS scores for 0-24 hours of
559 precipitation forecast from control trials (orange) and ADDRS data assimilation impact trials (green).

560 6. Summary

561 Distinct from operational balloon soundings, ADDRS created a new model, which is achieved a three-
562 phase sounding at one launch by effectively incorporating ascent profile sounding, stratospheric drift and
563 descent soundings. As well as ADDRS represents a next-generation approach to acquiring upper-air data,
564 surpassing the 20th century operational method. We developed a multi-station real-time reception system
565 utilizing 'Internet cloud + Instruments terminal' technology. Additionally, uplink commands can be sent from
566 the ground to facilitate descent measurements in designated areas and targeted observations in weather-sensitive
567 regions. Following over five years of extensive research and numerous field tests, the instruments, software, and
568 operational guidelines of the system have achieved a refined level of maturity. Starting January 1, 2024,
569 ADDRS already undergo operational experiments at four radiosonde observations stations in Guangdong, China.
570 Since July 2024, a planned operational trial at 127 CMA radiosonde observations stations aims to achieve full
571 operational capability across all CMA radiosonde observations stations by 2026. ADDRS is a situational
572 profiling technique that offers cost-effective upper-air measurements, making it suitable for widespread
573 application in operational soundings. However, challenges remain, such as improving the drift success rate,
574 enhancing relevant technologies, and fully leveraging the potential of continuous measurement data during the
575 drift phase. With the constant development of ADDRS and the continuous deepening of the measurement data,
576 ADDRS will become a development direction for future operational upper-air observation applications and
577 scientific research.

578

579 Data availability: Due to its proprietary nature <or ethical concerns>, supporting data cannot be made openly
580 available. Further information about the data and conditions for access are available at the [National Earth
581 System Science Data Center] at[<https://www.geodata.cn/collect/site/#/>].

582 Xiaozhong Cao¹, Qiyun Guo², Haowen Luo², Rongkang Yang², Peng Zhang², Guo Jianping³, Jincheng
583 Wang⁴, Die Xiao⁵, Jianping Du⁶, Zhongliang Sun⁷, Shijun Liu⁸, Sijie Chen⁹, Anfan Huang²

584

585 Author contributions. XC, QG and HL designed the experiments and wrote the paper; JW, DX, JD, ZS, SL
586 carried out the experiments; RY, JW analyzed the experimental results. PZ, GJ, SC, AH revised the paper and
587 participated in the discussion.

588 Competing interests. The contact author has declared that none of the authors has any competing interests.

589 Disclaimer. Publisher's note: Copernicus Publications remains neutral with regard to jurisdictional claims made
590 in the text, published maps, institutional affiliations, or any other geographical representation in this paper.
591 While Copernicus Publications makes every effort to include appropriate place names, the final responsibility
592 lies with the authors.

593 Financial support. This research has been supported by the National Natural Science Foundation of China (grant
594 no. U2442214) ; the National Key Research and Development Program (grant no. 2018YFC1506200) ;the
595 Innovation Team of the China Meteorological Administration(grant no. CMA2023QN11)..

596

597 REFERENCES

- 598 Anand, D., Kumar, B. S., and Ojha, D.: TIFR Zero-Pressure balloon program crosses a milestone, *Current*
599 *Science*, 2021, 120, 1672-1678, doi:<https://doi.org/10.18520/cs/v120/i11/1672-1678>.
- 600 Bauer, P., Thorpe, A., Brunet, G.: The quiet revolution of numerical weather prediction, *Nature*, 2015, 525, 47–
601 55, doi:<https://doi.org/10.1038/nature14956>.
- 602 Bormann, N., Lawrence, H., Farnan, J.: Global observing system experiments in the ECMWF assimilation
603 system, *ECMWF Technical Memorandum* 2019, 839, 24 pp., doi:<https://doi.org/10.21957/sr184iyz>.
- 604 Brown, D., Linz, M. & Leidich, J. Seasonal and geographic viability of high altitude balloon navigation. *Sci*
605 *Rep* 14, 21861 (2024). doi:<https://doi.org/10.1038/s41598-024-71445-9>.
- 606 Cohn, S. A., and Coauthors, 2013: Driftsondes: Providing In Situ Long-Duration Dropsonde Observations over
607 Remote Regions. *Bull. Amer. Meteor. Soc.*, 94, 1661–1674, doi:[https://doi.org/10.1175/BAMS-D-12-](https://doi.org/10.1175/BAMS-D-12-00075.1)
608 00075.1.
- 609 Cao, X. Z., Xia, Y. C., Luo, H. W., Liu, L. H., Liu, Y. F., Liu, Z. Y., Li, X., Guo, R., and Guo, Q. Y.: Technical
610 development and prospect of meteorological sounding measurement, *J. Adv. Meteorol. Sci. Technol*, 12,
611 27-36, 2022, doi:<https://doi.org/10.3969/j.issn.2095-1973.2022.05.005>.(in Chinese)
- 612 Cao, X. Z., Guo, Q. Y., Yang, R. K.: Research of rising and falling twice sounding based on long-time interval
613 of flat-floating, *Chinese Journal of Scientific Instrument*, 2019,40(2): 198-204.
614 <http://yqyb.etmchina.com/yqyb/article/abstract/20190223?st=search>. (in Chinese)
- 615 DuBois, J. L., Multhaupt, R. P., and Ziegler, C. A.: Invention and Development of the Radiosonde with a Catalog
616 of Upper-Atmospheric Telemetering Probes in the National Museum of American History, Smithsonian
617 Institution, *Smithsonian Studies in History and Technology*, 2002, 53, 1-78,
618 doi:<https://doi.org/10.5479/si.00810258.53.1>.
- 619 Fujiwara, M., Sun, B., Reale, A., Cimini, D., Larosa, S., Borg, L., von Rohden, C., Sommer, M., Dirksen, R.,
620 Maturilli, M., Vömel, H., Kivi, R., Ingleby, B., Kramer, R. J., Demoz, B., Madonna, F., Carminati, F.,
621 Lewis, O., Candy, B., Thomas, C., Edwards, D., Noersomadi, Shimizu, K., and Thorne, P.: Justification for
622 high-ascent attainment for balloon radiosonde observations at GRUAN and other sites, *Atmos. Meas.*
623 *Tech.*, 2025, 18, 2919–2955, doi:<https://doi.org/10.5194/amt-18-2919-2025>.
- 624 Gallice, A., Wienhold, F. G., Hoyle, C. R., Immler, F., and Peter, T.: Modeling the ascent of sounding balloons:
625 derivation of the vertical air motion, *Atmos. Meas. Tech.*, 2011, 4, 2235-2253,
626 doi:<https://doi.org/10.5194/amt-4-2235-2011>.
- 627 Gong, N., Liu, Y. F., Ren, J., Wu, Q., and Hu, H. L.: A Novel Adaptive Resource Allocation Framework for
628 Sounding Networks, 2021 the 11th International Workshop on Computer Science and Engineering (WCSE
629 2021) 276-283, doi:<https://doi.org/10.18178/wcse.2021.06.040>.
- 630 Guo, Q. Y., Yang, J. C., Yang, R. K., Qian, Y., and Cao, X. Z.: Evaluation of wind performance of domestic
631 Beidou dropsonde of ball-loading, *J. Nanjing Univ. Inf. Eng.: Nat. Sci. Ed.*, 10,
632 12, doi:<https://doi.org/10.13878/j.cnki.jnuist.2018.05.014>, 2018.(in Chinese)
- 633 Gong, J. D., Liu, Y. Z., Zhang, L.: A study of simplification and linearization of the NSAS deep convection
634 cumulus parameterization scheme for 4D-Var, *Acta Meteorologica Sinica*, 2019, 77, 595-616,
635 doi:<https://doi.org/10.11676/qxxb2019.048>.(in Chinese)

636 Haig, T. O., and V. E. Lally, 1958: Meteorological Sounding Systems. *Bull. Amer. Meteor. Soc.*, 39, 401–
637 409, doi:<https://doi.org/10.1175/1520-0477-39.8.401>.

638 He, Y., Zhu, X., Sheng, Z., and He, M.: Identification of stratospheric disturbance information in China based
639 on the round-trip intelligent sounding system, *Atmos. Chem. Phys.*, 2024, 24, 3839–3856,
640 doi:<https://doi.org/10.5194/acp-24-3839-2024>.

641 Hersbach, H., Bell, B., Berrisford, P., Hirahara, S., Horányi, A., Muñoz - Sabater, J., Nicolas, J., Peubey, C.,
642 Radu, R., Schepers, D., Simmons, A., Soci, C., Abdalla, S., Abellan, X., Balsamo, G., Bechtold, P., Biavati,
643 G., Bidlot, J., Bonavita, M., De Chiara, G., Dahlgren, P., Dee, D., Diamantakis, M., Dragani, R., Flemming,
644 J., Forbes, R., Fuentes, M., Geer, A., Haimberger, L., Healy, S., Hogan, R. J., Hólm, É., Janisková, M.,
645 Keeley, S., Laloyaux, P., Lopez, P., Lupu, C., Radnoti, G., de Rosnay, P., Rozum, I., Vamborg, F.,
646 Villaume, S., Thépaut, J. - N.: The ERA5 global reanalysis, *Q. J. R. Meteorolog.*
647 *Soc.*, doi:<https://doi.org/10.1002/qj.3803>, 2020.

648 Ingleby, B., and Coauthors, 2016: Progress toward High-Resolution, Real-Time Radiosonde Reports. *Bull.*
649 *Amer. Meteor. Soc.*, 97, 2149–2161, doi:<https://doi.org/10.1175/BAMS-D-15-00169.1>.

650 Ingleby, B., Rodwell, M., Isaksen, L.: Global radiosonde network under pressure, ECMWF Newsletter No. 149
651 – Autumn 2016, pp. 25 - 30, doi:<https://www.ecmwf.int/sites/default/files/elibrary/2016/18147-global-radiosonde-network-under-pressure.pdf>.

652
653 Ingleby, B., 2021: Use of radiosonde descent data from ships, ECMWF Newsletter, Page 5
654 doi:[https://www.ecmwf.int/sites/default/files/elibrary/102021/20225-newsletter-no-169-autumn-](https://www.ecmwf.int/sites/default/files/elibrary/102021/20225-newsletter-no-169-autumn-2021_1.pdf)
655 [2021_1.pdf](https://www.ecmwf.int/sites/default/files/elibrary/102021/20225-newsletter-no-169-autumn-2021_1.pdf).

656 Ingleby, B., Motl, M., Marlton, G., Edwards, D., Sommer, M., von Rohden, C., Vömel, H., and Jauhiainen, H.:
657 On the quality of RS41 radiosonde descent data, *Atmos. Meas. Tech.*, 2022, 15, 165-
658 183, doi:<https://doi.org/10.5194/amt-15-165-2022>.

659 Johnson, A., Wang, X., Hutchinson, T., and Creus-Costa, J.: Impact of WindBorne observation assimilation on
660 prediction of a TPV merger case from THINICE, *J. Geophys. Res. Atmospheres*, 2024, 129,
661 e2024JD041395, doi:<https://doi.org/10.1029/2024JD041395>.

662 Jensen, M. P., Holdridge, D. J., Survo, P., Lehtinen, R., Baxter, S., Toto, T., and Johnson, K. L.: Comparison of
663 Vaisala radiosondes RS41 and RS92 at the ARM Southern Great Plains site, *Atmos. Meas. Tech.*, 2016, 9,
664 3115–3129, doi:<https://doi.org/10.5194/amt-9-3115-2016>.

665 Liu, S. J., Yang, R. K., Cao, X. Z., Guo, Q. Y., Cheng, K. Q., Kan, Z. P., and Wang, J. C.: Analysis and
666 Numerical Experiment of the Horizontal Drift Round-trip Sounding Balloon's Dynamic and Thermal
667 Process in the Adjacent Space, *Chin. J. Atmos. Sci.*, 2022, 46, 788–
668 804, doi:<https://doi.org/10.3878/j.issn.1006-9895.2110.20252>.(in Chinese)

669 Liu, Y. F., Zhou, Y. Y., Du, J. P., Liu, D., Ren, J., Chen, Y. H., Zhang, F., and Chen, J. P.: RTP-GRU:
670 Radiosonde Trajectory Prediction Model Based on GRU, in *Proceedings.*, 2021, 24, 10.1007/978-981-15-
671 8462-6_61.

672 Liu, L. H.; Han, Y.; Xia, Y. C.; Guo, Q. Y.; Gao, W.; Guo, J. P.: Investigation of Atmospheric Dynamic and
673 Thermodynamic Structures of Typhoon Sinlaku (2020) from High-Resolution Dropsonde and Two-Way
674 Rawinsonde Measurements. *Remote Sens.* 2022, 14, 2704. doi:<https://doi.org/10.3390/rs14112704>.

675 Lau, D.S., Chan, W.S., Wong, Y.C., Lam, C.C., Chan, P.W.: Hindcast Insights from Storm Surge Forecasting of
676 Super Typhoon Saola (2309) in Hong Kong with the Sea, Lake and Overland Surges from Hurricanes
677 Model, *Atmos.*, 2024, 15, 17, doi:<https://doi.org/10.3390/atmos15010017>.

678 Majumdar, S.J.: A review of targeted observations, *Bull. Am. Meteorol. Soc.*, 2016, 97, 2287-
679 2303, doi:<https://doi.org/10.1175/BAMS-D-14-00259.1>.

680 Magnusson, L., Majumdar, S.J., Dahoui, M.L., Bormann, N., Bonavita, M., Browne, P.A., Brown, A.R., De
681 Chiara, G., Duncan, D.I., English, S., Geer, A.J., Healy, S., Ingleby, B., McNally, A.P., Pappenberger, F.,
682 Prates, F., Rabier, F., de Rosnay, P., Rennie, M.P., Warrick, F.: The role of observations in ECMWF
683 tropical cyclone initialisation and forecasting, *Q. J. R. Meteorolog. Soc.*, 2025, 151(768),
684 e4924, doi:<https://doi.org/10.1002/qj.4924>.

685 Pettifer, R. E.: From Observations to Forecasts - Part 2. The development of in situ upper air measurements,
686 *Weather*, 2009, 64, doi:<https://doi.org/10.1002/wea.484>.

687 Raman, M. R., Ratnam, M. V., Rajeevan, M., Rao, V. V. M. J., Rao, S. V. B.: Intriguing Aspects of the
688 Monsoon Low-Level Jet over Peninsular India Revealed by High-Resolution GPS Radiosonde
689 measurements, *J. Atmos. Sci.*, 2011, 68, 1413–1423, doi:<https://doi.org/10.1175/2011JAS3611.1>.

690 Roth, S., & Yoder, C. D.: Balloon missions soar to new heights. *Aerospace America*, 2022, 60(11), 35-35.
691 doi:<https://aerospaceamerica.aiaa.org/year-in-review/balloon-missions-soar-to-new-heights>.

692 Ratnam, M. V., Pravallika, N., Babu, S. R., Basha, G., Pramitha, M., Murthy, B. V. K.: Assessment of GPS
693 radiosonde descent data, *Atmos. Meas. Tech.*, 2014, 7(4), doi:<https://doi.org/10.5194/amt-7-1011-2014>.

694 Seidel, D. J., Berger, F. H., Diamond, H. J., Dykema, J., Goodrich, D., Immler, F., Murray, W., Peterson, T.,
695 Sisterson, D., Sommer, M., Thorne, P., Vomel, H., & Wang, J.: Reference Upper-Air Observations for
696 Climate: Rationale, Progress, and Plans. *Bulletin of the American Meteorological Society*, 2009, 90(3),
697 361-369. doi:<https://doi.org/10.1175/2008BAMS2540.1>

698 Shen, Z. P., Pan, X. Z., and Yi, Y. L.: Preparation and properties of modified nano-clay/natural latex composites,
699 *J. Rubber Ind.*, 2020, 67, 4, doi:<https://doi.org/10.12136/j.issn.1000-890X.2020.08.0580>.(in Chinese)

700 Tan, X. W., Chen, D. H., Zhang, Q. H.: An impact study of a new type of data of adaptive or targeting
701 observation on typhoon forecast, *J. Trop. Meteorol.*, 2006, 22(1), 18 –
702 25, doi:<https://doi.org/10.3969/j.issn.1004-4965.2006.01.003>.(in Chinese)

703 Vernier, J. - P., Fairlie, T. D., Deshler, T., Ratnam, M. V., Gadhavi, H., Kumar, B. S., Natarajan, M., Pandit, A.
704 K., Raj, S. T. A., Kumar, A. H., Jayaraman, A., Singh, A. K., Rastogi, N., Sinha, P. R., Kumar, S., Tiwari,
705 S., Wegner, T., Baker, N., Vignelles, D., Stenchikov, G., Shevchenko, I., Smith, J., Bedka, K., Kesarkar, A.,
706 Singh, V., Bhate, J., Ravikiran, V., Rao, M. D., Ravindrababu, S., Patel, A., Vernier, H., Wienhold, F. G.,
707 Liu, H., Knepp, T. N., Thomason, L., Crawford, J., Ziemba, L., Moore, J., Crumeeyrolle, S., Williamson,
708 M., Berthet, G., Jégou, F., Renard, J. B.: BATAL: The Balloon Measurement Campaigns of the Asian
709 Tropopause Aerosol Layer, *Bull. Am. Meteorol. Soc.*, 2018, 99, 955–
710 973, doi:<https://doi.org/10.1175/BAMS - D - 17 - 0014.1>.

711 Vernier, H., Rastogi, N., Liu, H., Pandit, A. K., Bedka, K., Patel, A., Ratnam, M. V., Kumar, B. S., Zhang, B.,
712 Gadhavi, H., Wienhold, F., Berthet, G., and Vernier, J.-P.: Exploring the inorganic composition of the
713 Asian Tropopause Aerosol Layer using medium-duration balloon flights, *Atmos. Chem. Phys.*, 2022, 22,
714 12675–12694, doi:<https://doi.org/10.5194/acp-22-12675-2022>.

715 WMO (World Meteorological Organization): 8th WMO Workshop on the Impact of Various Observing Systems
716 on Numerical Weather Prediction and Earth System Prediction, Norrköping, Sweden, 27 - 30 May 2024,
717 doi:<https://community.wmo.int/en/meetings/8th-wmo-impact-workshop-home>.

718 Wang, J. H. , Young, K., Hock, T., Lauritsen, D., Behringer, D., Black, M., Black, P. G., Franklin, J., Halverson,
719 J., Molinari, J., Nguyen, L., Reale, T., Smith, J., Sun, B., Wang, Q., Zhang, J. A.: A long-term, high-quality,
720 high-vertical resolution GPS dropsonde data set for hurricane and other studies, *Bull. Am. Meteorol. Soc.* ,
721 2015, 96, 961-973, doi:<https://doi.org/10.1175/BAMS-D-13-00203.1>.

722 WMO (World Meteorological Organization): Guide to Meteorological Instruments and Methods of Observation,
723 Volume III - Observing Systems, WMO-No. 8, 2025 edition, Page 464, pp.,
724 doi:<https://library.wmo.int/idurl/4/41650>.

725 WMO (World Meteorological Organization): Instruments and Observing Methods Report No. 143: Report of
726 WMO's 2022 Upper-Air Instruments Intercomparison Campaign, Geneva, 2024, 22
727 pp., doi:<https://library.wmo.int/idurl/4/68808>.

728 WMO (World Meteorological Organization): The gaps in the Global Basic Observing Network (GBON), SOFF
729 Series No. 2, 2020, Page 4, pp., doi:<https://library.wmo.int/idurl/4/57174>.

730 Wang, D., Wang, J. C., Tian, W. H., Guo, Q. Y.: Quality control and uncertainty analysis of Round - trip
731 drifting sounding system data, *Chinese J. Atmos. Sci.*, 2020, 44,
732 20, doi:<https://doi.org/10.3878/j.issn.1006-9895.1912.19203>. (in Chinese)

733 Wang, R. W., Han, W., Tian, W. H., Gong, J. D.: Blacklist Design of AMDAR Temperature Data and Their
734 Application in the CMA-GFS, *J. Trop. Meteorol.*, 2021, 27, 368–377, doi:<https://doi.org/10.46267/j.1006-8775.2021.032>.

736 Wang, F., Gong, J. D., Wang, R. C., Chen, Y. D.: A methodological study of the CMA global hybrid four-
737 dimensional variational data assimilation system, *Acta Meteorol. Sin.*, 2024, 82(5), 709–
738 720, doi:<https://qxxb.cmsjournal.net/cn/article/doi/10.11676/qxxb2024.20230140>. (in Chinese)

739 Wang, R. W., Wang, J. C., Wang, D., Tao, Y. W., Tian, W. H.: Study on the Influence of Return Sounding
740 Observation System Based on CMA-MESO, *Meteorol. Mon.*, 2023, 49(1), 52–
741 61, doi:<https://doi.org/10.7519/j.issn.1000-0526.2022.032601>. (in Chinese)

742 Wang, J. C., Wang, D., Wang, R. W., Tan, J., Rong, N.: Assimilation of Round-Trip Horizontal Drift
743 Radiosonde Data in CMA-MESO 3DVar and Its Impact on Model Forecast, *Meteorol. Mon.*, 2024, 50(2),
744 50–60, doi:<https://doi.org/10.7519/j.issn.1000-0526.2023.110501>. (in Chinese)

745 Wang, J. C., Wang, D., Yang, R. K., Cao, X. Z., Guo, Q. Y.: A Return Radiosonde Trajectory Forecast Method
746 and Its Preliminary Evaluation Based on High Resolution Numerical Weather Prediction Model, *Chinese J.*
747 *Atmos Sci.*, 2021, 45, 651–663, doi:<https://doi.org/10.3878/j.issn.1006-9895.2012.20186>.

748 Wen, Q. S., Zhang, X. F., Hu, S., Zhao, P. T., Zhong, S. X., Liu, Z. Y., Zhao, Z. K., Liang, J. H., Dai, G. F.,
749 Zhang, C. Z., Li, M. J., Huang, L.: Collaborative assimilation experiment of Beidou radiosonde and drone-
750 dropped radiosonde based on CMA-TRAMS, *Atmos. Oceanic Sci. Lett.*, 2025,
751 18(2), doi:<https://doi.org/10.1016/j.aosl.2024.100555>.

752 Xu, H. F., Guo, Q. Y., Liu, Y. Z., et al.: Key factors influencing drift success rate of new-type meteorological
753 balloons, *Journal of Applied Meteorological Science*, 2025, 36(4), 427-440.
754 doi:<https://doi.org/10.11898/1001-7313.20250404>.(in Chinese)

755 Yang, R. K., Wang, Y., and Liu, Q. Q.: Dynamic Performance Analysis of Sounding temperature sensor, Sci.
756 Technol. Eng.,2014, doi:<https://doi.org/10.3969/j.issn.1671-1815.2014.04.012>.(in Chinese)

757 Yang, J. C., et al: Research on error prediction technology of radiosonde temperature sensor, Journal of
758 Electronic Measurement and Instrumentation, 2022, 35(12):24-26.
759 doi:<https://doi.org/10.13382/j.jemi.B2104288>.(in Chinese)

760 Yang, C. Y., Guo, Q.Y., Cao, X.Z., Zhang, W.: Analysis of gravity wave characteristics in the lower
761 stratosphere based on new round-trip radiosonde. Acta Meteorologica Sinica, 2021, 79(1):150-167.
762 doi:<https://doi.org/10.11676/qxxb2021.008>.(in Chinese)

763 Yang, C. Y., Cao, X.Z., Guo, Q.Y., et al. : Feature Extraction and Analysis of Atmospheric Turbulence Based
764 on New Round-Trip Radiosonde [J]. Chinese Journal of Atmospheric Sciences (in Chinese), 2023, 47(6):
765 1967–1982. doi:<https://doi.org/10.3878/j.issn.1006-9895.2202.21103>.(in Chinese)

766 Zhu, H. J., Li, F. Z., Kan, Z. P., He, H., Xiao, D. E., Zhang, L. Q.: Latex balloons buoyancy change analysis and
767 vertical motion trajectory simulation, J. Rubber Ind., 2021, 68(8). doi:<https://doi.org/10.12136/j.issn.1000-890-x.2021.01.0017>. (in Chinese)

769 Zhang, X. P., Guo, Q. Y., Yang, R. K., Ma, X. L., Cao, X. Z.: Assimilation Experiment of Rainstorm in the
770 Middle and Lower Reaches of the Yangtze River Based on "ascent - drift - descent" Sounding Data,
771 Meteorol. Mon., 2021, 47(12), 1512–1524, doi:<https://doi.org/10.7519/j.issn.1000-0526.2021.12.007>. (in
772 Chinese)

773 Zhou, X. S., Guo Q.Y., Xia Y.C., et al.: Inspection of FY-3D satellite temperature data based on horizontal drift
774 round-trip sounding data. J Appl Meteor Sci, 2023, 34(1): 52-64. DOI: 10.11898/1001-7313.20230105.(in
775 Chinese)

776 Zhou, X. S., Hong G., Xia Y.C., Luo H.W., Bao W.Z., Tian H.,: Verification of FY-3D Satellite Humidity
777 Profiles Using Descending Phase Data of Round-Trip Drifting Sounding[J].Meteor Mon, 2024,
778 50(11):1373-1385, <http://dx.doi.org/10.7519/j.issn.1000-0526.2024.063002>. (in Chinese)

779 Zhang, C. Z ., et al.,: Application Experiment of Assimilating Beidou Satellite Navigation Round-Trip Sounding
780 Data Observed in Guangdong Province Using CMA-GD Model, Journal of Tropical Meteorology, 2025,
781 41(1) ,16-25,doi:<https://doi.org/10.16032/j.issn.1004-4965.2025.001>.(in Chinese)

782 Zhang, X, Wang Q. P, MA, X.L, et al. ,: The Influence of New Round-Trip Drifting Sounding Observation on
783 the Quality of Numerical Prediction in the Middle and Lower Reaches of the Yangtze River [J]. Chinese
784 Journal of Atmospheric Sciences, 2025, 49(1): 245–256. doi:<https://doi.org/10.3878/j.issn.1006-9895.2304.22224>.(in Chinese)

785

786 Zhang, X. P., Sun, L., Ma, X. L., et al.: Can the Assimilation of the Ascending and Descending Sections' Data
787 from Round-Trip Drifting Soundings Improve the Forecasting of Rainstorms in Eastern China?
788 Atmosphere., 2023, 14, 1127. doi: <https://doi.org/10.3390/atmos14071127>.

789 Zhuang, Z. R., Wang, R. C., Wang, J. C., Gong, J. D.: GRAPES_Meso background error characteristics and
790 application, J. Appl. Meteorol. Sci., 2019, 30(3), 316–331, doi:<https://doi.org/10.11898/1001-7313.20190306>. (in Chinese)

791

792 Zhang, X. F., Li, L. X., Yang, R. K., et al.: Comprehensive Marine Observing Experiment Based on High-
793 Altitude Large Unmanned Aerial Vehicle (South China Sea Experiment 2020 of the “Petrel Project”). Adv.
794 Atmos. Sci. 38, 531–537 (2021). doi:<https://doi.org/10.1007/s00376-020-0314-1>.